



## RESEARCH ARTICLE

10.1029/2018JB015979

## Key Points:

- Lithospheric structures beneath Jeju Island were imaged by teleseismic travelttime tomography for the first time
- Low-velocity anomalies show dispersed magmatic structures within the lithosphere, corresponding to surface features of volcanism
- The focused decompressional melting was attributed to the transition of lithospheric thickness beneath the island

## Supporting Information:

- Supporting Information S1

## Correspondence to:

J. Rhie,  
rhie@snu.ac.kr

## Citation:

Song, J.-H., Kim, S., Rhie, J., Lee, S.-H., Kim, Y., & Kang, T.-S. (2018). Imaging of lithospheric structure beneath Jeju Volcanic Island by teleseismic travelttime tomography. *Journal of Geophysical Research: Solid Earth*, 123. <https://doi.org/10.1029/2018JB015979>

Received 18 APR 2018

Accepted 23 JUL 2018

Accepted article online 31 JUL 2018

## Imaging of Lithospheric Structure Beneath Jeju Volcanic Island by Teleseismic Travelttime Tomography

Jung-Hun Song<sup>1</sup> , Seongryong Kim<sup>1</sup> , Junkee Rhie<sup>1</sup> , Sang-Hyun Lee<sup>1</sup> , YoungHee Kim<sup>1</sup> , and Tae-Seob Kang<sup>2</sup>

<sup>1</sup>School of Earth and Environmental Sciences, Seoul National University, Seoul, South Korea, <sup>2</sup>Department of Earth and Environmental Sciences, Pukyong National University, Busan, South Korea

**Abstract** Jeju Island (JI) is an intraplate volcanic field located at the continental margin of Northeast Asia. This volcanic island has been formed by multiple eruptions from the Pleistocene to the Holocene (~3.7 ka), which have yielded hundreds of monogenetic volcanic cones and a central basaltic shield. To understand the volcanic structures and mechanism beneath JI, we deployed 20 broadband temporary seismometers across the island for over two years (October 2013 to November 2015). We investigated the crustal and upper mantle structures in JI for the first time using the gathered data. Through teleseismic travelttime tomography, we obtained images of the lithospheric structure related to the volcanic system. A major finding was the identification of a prominent low-velocity anomaly (<−0.3 km/s in *P* wave velocity relative to the surrounding high-velocity region) beneath the summit of the central shield volcano at greater depths (50–60 km), which separates into low-velocity zones at shallower depths (10–45 km). Based on previous geological observations, the anomalies were interpreted as a magmatic system, potentially with partial melting. Moreover, relatively high velocity zones were consistently imaged to the north, east, and west of the island, indicating relatively thick lithospheric structures at the southern margin of the continental lithosphere beneath the Korean Peninsula. Based on the geometries of the imaged structures, we suggest that a focused decompressional melting at sublithospheric depths and complex magma interactions within the lithosphere resulted in the characteristics of JI volcanism as intraplate magmatic activities that are isolated in space and confined in time.

### 1. Introduction

Small-scale magmatic systems are often expressed at the Earth's surface as a monogenetic volcanic field (Smith & Németh, 2017), where individual volcanoes are active for a short duration, erupt small volumes of magma (Németh & Keresztsuri, 2015), have a variety of eruptive styles, and display systematic changes of geochemical compositions (Brenna et al., 2010, 2011; Németh, 2010). Although this volcanic system is common in different intraplate settings (Connor & Conway, 2000; Le Corvec et al., 2013), the origin and evolution of magmatism in such a system are not well understood. This is due to a lack of information about the melt focusing process in the lithospheric and sublithospheric upper mantle and about heterogeneous interactions of the magma with the surrounding lithosphere and tectonic structures (Brenna, Cronin, et al., 2015; Cañón-Tapia & Walker, 2004; Hoernle et al., 2006; Smith & Németh, 2017).

Jeju Island (JI) is a Cenozoic volcanic field situated off the south coast of the Korean Peninsula. Volcanoes have erupted episodically from the Pleistocene (~1.8 Ma) to the Holocene (~3.7 ka), yielding more than 300 small-scale volcanoes of different types, including scoria cones, tuff rings, tuff cones, and lava domes and a central basaltic shield in a confined area ( $75 \times 32 \text{ km}^2$ ). JI is formed in an intraplate setting, and several hypotheses have been put forward to explain its formation mechanism (e.g., Brenna, Cronin, et al., 2015; M. W. Lee, 1982; Nakamura et al., 1990; Shin et al., 2012; Tatsumi et al., 2005; see section 5.3 for further details). However, due to a lack of geophysical studies, the origin and magmatic processes of volcanism in JI have not been confirmed.

Tomographic approaches using data on the relative travelttime of teleseismic body waves have been used to image upper mantle structures from continental scales (e.g., Argnani et al., 2016; Biryol et al., 2011; Schmandt & Lin, 2014) to regional scales (e.g., Bastow et al., 2008; Rawlinson & Kennett, 2008; Schlömer et al., 2017). This method has been successful in revealing detailed three-dimensional (3-D) velocity heterogeneities beneath seismic arrays by taking advantage of individual rays from a common event sharing the same path outside of

©2018. The Authors.

This is an open access article under the terms of the Creative Commons Attribution-NonCommercial-NoDerivs License, which permits use and distribution in any medium, provided the original work is properly cited, the use is non-commercial and no modifications or adaptations are made.

the region of interest and sampling velocity variations inside the modeled space (Aki et al., 1977; Lévéque & Masson, 1999; Thurber, 2003). This method has provided useful information on unrevealed localized upper mantle structures, for example, in Northeast (NE) Asia (e.g., Chen et al., 2017; Lei & Zhao, 2005; Ma et al., 2018; Zhao et al., 2009). However, care must be taken when interpreting results from this method despite its ability to resolve horizontal velocity contrast. As the approach uses rays with subvertical trajectories, vertical velocity contrasts are not well constrained due to vertical smearing, effects by unresolved surface structures in the model space, and potential influence by heterogeneous velocity structures below the model region (Rawlinson et al., 2006; Zhao et al., 2013). Therefore, a comprehensive analysis is necessary to ensure robust images by incorporating prior knowledge about the geology and tectonics of the region and meticulous recovery experiments to test the obtained features of velocity anomalies.

In this study, we applied the above method to image the lithospheric structure related to the intraplate volcanism in JI. To this end, we deployed 20 temporary broadband stations across the island for a period of over 2 years (October 2013 to December 2015). Relative arrival time differences between seismic stations were measured by the adaptive stacking procedure (Rawlinson & Kennett, 2004), using selected high-quality teleseismic waveforms from the recordings of the network. With resolution analysis using various synthetic models, it was possible to estimate reliable 3-D crust and upper mantle velocity structures beneath JI for the first time, which provided insights into the magmatic processes related to the intraplate volcanism in the island.

## 2. Geological Setting and History

JI is located at the southeastern margin of the continental lithosphere in NE Asia (Figure 1a). The major tectonic boundaries surrounding JI are the Ryukyu trench, about 650 km to the southeast, and the Japan Trench further to the east, formed by the subduction of the Philippine Sea plate (Nakamura et al., 1989) and Pacific plate (Sager et al., 1988), respectively, beneath the Eurasian plate. Several arc volcanoes are located near the trenches, and intraplate volcanoes, including JI, are sporadically distributed in the Eurasian plate away from the plate boundaries.

JI and the Korean Peninsula have experienced a similar tectonic evolution during the Mesozoic and Cenozoic (Chough et al., 2000; K. H. Kim et al., 2002; Sager et al., 1988; Yang et al., 2010). In the Cretaceous, the regions were part of the arc-back-arc system associated with the subduction of the proto-Pacific (Izanagi) plate beneath the continental lithosphere (Chough et al., 2000). Since the Late Cretaceous to early Tertiary, the rollback of the subducting plate led to a change to a back-arc extensional environment with the emplacement of calc-alkaline magmatism (Chough & Sohn, 2010; K. H. Kim et al., 2002; Woo et al., 2014). The opening of the Cenozoic back-arc basins, for example, East Sea and East China Sea, occurred between 27 and 15 Ma (Chough et al., 2000; Otofuji et al., 1985), and JI and the Korean Peninsula transitioned from a back-arc to intraplate tectonic system.

The volcanic island was formed by cumulative and sequential volcanic eruptions since the Late Pleistocene, showing complex variations in geochemical and eruption patterns (Brenna et al., 2011; Brenna, Cronin, Smith, Sohn, & Maas, 2012; Sohn et al., 2012). By forming dispersed monogenetic volcanic cones and lava flows (Brenna, Cronin, Smith, Sohn, & Maas, 2012), the volcanism was initiated by hydrovolcanic activity (G. W. Koh et al., 2013; Sohn et al., 2008; Sohn & Park, 2004) on a continental shelf of granitic basement since the Pleistocene (~1.8 Ma; K. H. Kim et al., 2002). Subsequent large-volume lava effusion formed a composite shield along with hundreds of individual eruptive centers above the sea surface since the Middle Pleistocene (~0.5 Ma), and several tuff rings and tuff cones were formed during the Late Pleistocene and Holocene (Figure 1c; Brenna, Cronin, et al., 2015; G. W. Koh et al., 2013). Additional lava flows from evolved magma formed the uppermost part of the island consisting of Mt. Halla trachyte at about 25 ka (Brenna, Cronin, Smith, Sohn, & Maas, 2012), and subsequent basaltic eruptions covered the trachyte dome and flows, forming the current surface of the volcanic edifice (Ahn & Hong, 2017; J. S. Koh et al., 2003). It has been reported that there are many pyroclastic cones (more than 150) buried beneath the younger lavas (Sohn & Park, 2004, 2005). The volcanic activity lasted until recently based on dating (~3.7 ka) and historical records (~1 ka; Ahn, 2016; Sohn et al., 2015).

A small number of studies have elucidated the lithospheric structure beneath JI. The basement of the island consists of Jurassic-Cretaceous granites with layers of overlying Cretaceous-Tertiary rhyolitic tuff (Choi et al., 2006; K. H. Kim et al., 2002; Park et al., 2005; Tatsumi et al., 2005). The crustal thickness beneath the island

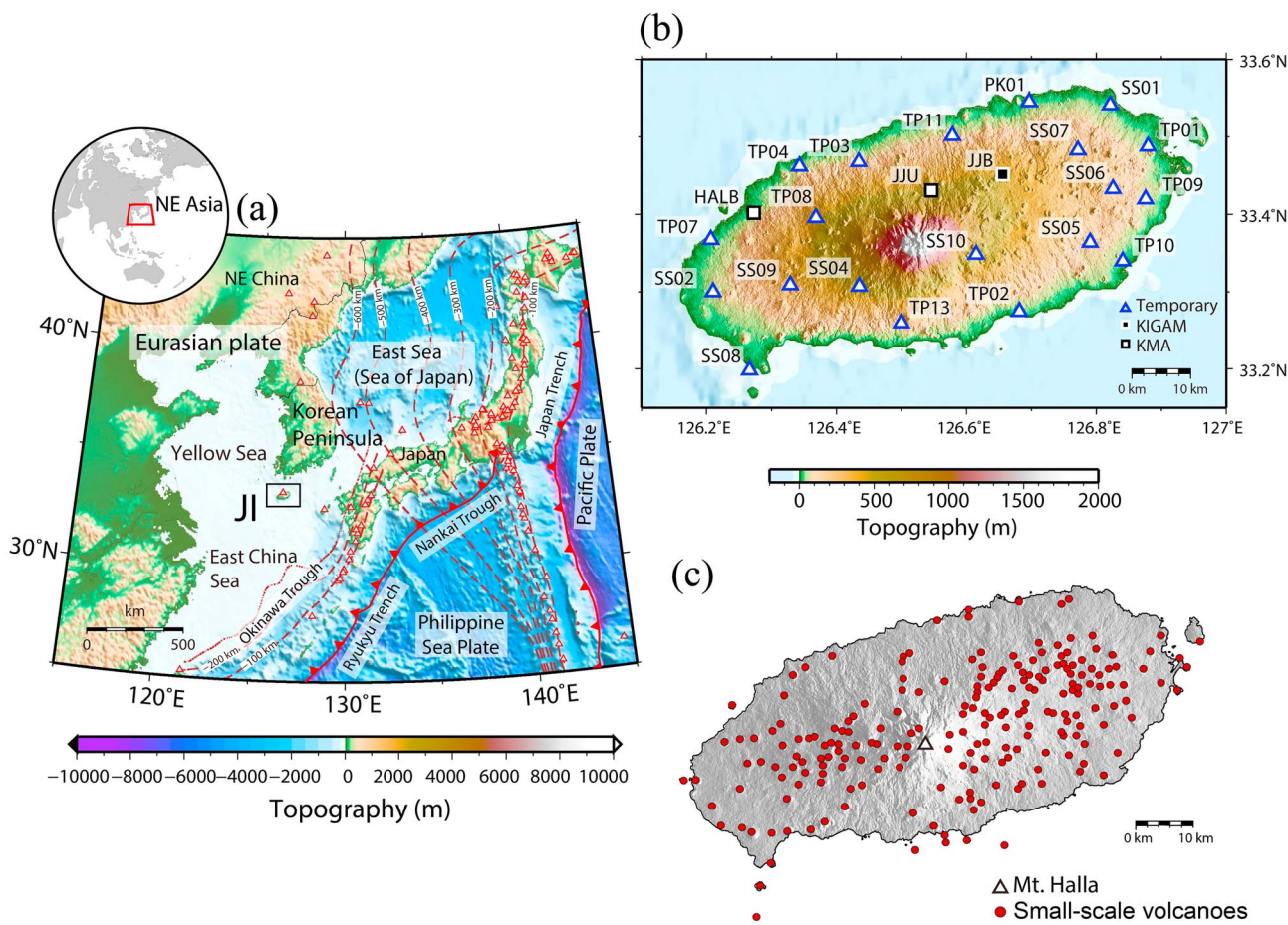


**Figure 1.** Maps of northeast (NE) Asia and Jeju Island (JI). (a) The location of JI is indicated by the black rectangular box. Slabs of oceanic plate are denoted by brown dashed contour lines at a 100-km depth interval (Iwasaki et al., 2015). Volcanoes in NE Asia are indicated by triangles. Convergent plate boundaries are shown with red saw-toothed lines (Bird, 2003). (b) Map of seismic stations used in this study. The 20 temporary stations are shown as triangles, and the three permanent stations operated by the Korea Institute of Geoscience and Mineral Resources (KIGAM) and Korea Meteorological Administration (KMA) are shown as black and white squares, respectively. (c) Distribution of small-scale volcanoes (e.g., scoria cones, tuff rings, tuff cones, and lava domes) on JI denoted by red dots. Mt. Halla, the central shield volcano, is denoted by the white triangle.

estimated by seismological studies varies from 24.8 to 35 km (Y. Kim et al., 2015; Yoo et al., 2007; Zheng et al., 2011). Gravity and magnetic anomaly data favor shallow Moho and mafic intrusions (Shin et al., 2012). The lithosphere is generally thin, not exceeding 60 km (Pasyanos et al., 2014).

### 3. Data and Method

#### 3.1. The 2013–2015 Jeju Seismic Array Network

From October 2013 to November 2015, we deployed 20 temporary broadband seismic stations to investigate the seismic activity and velocity structures beneath JI (Figure 1b). Twenty-three stations, including three permanent stations, namely, the JJJ and HALB of the Korea Meteorological Administration and the JJB of the Korea Institute of Geoscience and Mineral Resources, with an average spacing of 9 km across the island, provided the data during the study period. All temporary stations were equipped with Nanometrics Trillium compact broadband sensors with Taurus recorders and global positioning system clocks, continuously acquiring data at 200 samples per second for three individual components.

#### 3.2. Seismic Events

We selected 484 teleseismic events with magnitudes larger than mb 5.5 in an epicentral distance range of 30–95° from the Data Management Center of Incorporated Research Institutions for Seismology. Before examining the waveforms, instrument responses were removed from all recorded data to obtain actual

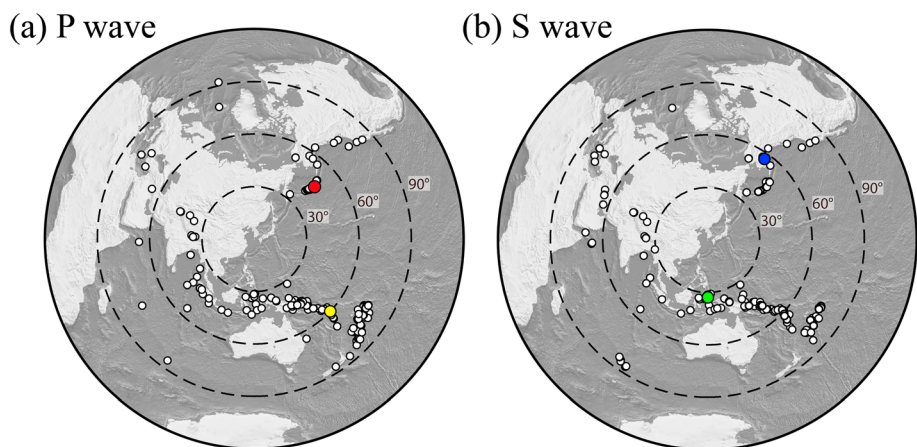


**Figure 2.** Distribution of teleseismic events (circles) used in tomographic inversion. All events were in distance range of 30–95° with  $mb > 5.5$ , recorded by the Jeju array from October 2013 to November 2015. (a)  $P$  wave sources (180 in total). Yellow and red circles indicate event locations of waveforms in Figures 3a and 3b, respectively. (b)  $S$  wave sources (161 in total). Green and blue circles indicate event locations of waveforms in Figures 3c and 3d, respectively. Black dashed circles indicate great-circle distances with 30° increments.

three-component ( $Z$ ,  $N$ , and  $E$ ) displacement signals. We used vertical component data to identify  $P$  waves and tangential component data to identify  $S$  waves. Two-pole Butterworth band-pass filters with corner frequencies of 0.1–5 and 0.05–0.2 Hz were applied for  $P$  and  $S$  waves, respectively. We visually inspected all the teleseismic waveforms and used only those with clear phase arrivals recorded at more than 13 stations measuring the relative arrival time residuals. Counting the direct  $P$  and  $S$  phases and the additional  $pP$ ,  $sP$ ,  $PP$ , and  $sS$  phases, we analyzed a total of 180 events for  $P$  waves and 161 for  $S$  waves (Figure 2).

### 3.3. Measurement of Relative Arrival Time Residual

Using the ak135 global reference model (Kennett et al., 1995), traces were preliminarily aligned with a theoretical phase arrival time. Traveltime residuals were then estimated by applying the adaptive stacking technique (Rawlinson & Kennett, 2004). This method calculates traveltimes by iteratively improving trace alignment based on the relative coherence of each waveform and the stacked reference waveforms. We used a time window with a width of 12 s in  $P$  waves and 25 s in  $S$  waves for stacking, which was wide enough to contain the initial phase arrivals. Then, 10 iterations were performed to obtain a reliable estimation of residuals. Depending on waveform conditions, we slightly adjusted the time window length and number of iterations. Finally, the residual mean was subtracted from the residual data for each event to obtain the relative residuals. Our final data set used in tomographic inversion comprised 3,345  $P$  and 2,570  $S$  wave residuals.

The uncertainties of the residual data were estimated by a similar approach as that described by Rawlinson and Kennett (2004). To measure the errors between the input time shifts and their recoveries by the adaptive stacking procedure, random time perturbations were applied to the aligned traces with a standard deviation of 0.2 s for  $P$  waves and 0.75 s for  $S$  waves. We repeated the test 100 times with the randomly perturbed synthetic data and obtained the final uncertainty measurements by taking the averages of the errors. We assumed that the level of uncertainties of each residual was not less than 5 ms (50% of sampling interval) to account for imperfect coherence of the records and data noise (Rawlinson & Kennett, 2004). We tested inversion with minimum uncertainties slightly higher than 5 ms (10 and 15 ms), but there were no significant changes in the final results (Figure S1 in the supporting information). The estimated uncertainty of each residual arrival time measurement was used as a weighting factor in tomographic inversion.

### 3.4. Tomographic Inversion

To estimate the 3-D velocity perturbations of  $P$  and  $S$  waves, we used the teleseismic tomography method of Rawlinson et al. (2006). It was assumed that the 3-D model volume beneath the seismic array consisted of regular grids in the spherical coordinate. Traveltimes in the local model were then predicted by a grid-based eikonal solver called the fast marching method (Rawlinson & Sambridge, 2004). An iterative nonlinear

tomographic process was carried out using a subspace inversion scheme (Kennett et al., 1988). Regularization factors (damping and smoothing) were applied during the inversion procedure.

For both  $P$  and  $S$  wave tomographic inversions, we defined the local model as spanning  $1.94^\circ$  in longitude,  $1.13^\circ$  in latitude, and 65 km in depth. A total of 14,560 nodes with grid spacing of 4.5 km in the horizontal direction ( $40 \times 28$  nodes) and 5.5 km in the vertical direction (13 nodes) was used to invert relative arrival time residuals. The spacing of grids and the maximum depth of the model space were determined based on resolution tests with synthetic data and inversion results using real data. We used the ak135 global reference velocity model (Kennett et al., 1995) for the initial velocities of each grid node. We performed only 10 iterations during the inversion process, noting that more iterations did not result in significant improvements in data variance and model features. We determined the optimum values of damping (10.0 for  $P$  wave and 50.0 for  $S$  wave tomography) and smoothing (5.0 for  $P$  wave and 10.0 for  $S$  wave tomography) based on trade-off curve analyses (Figure S2). Station elevations were corrected during the inversion process and station correction terms were included in the tomographic inversions so that the results were less affected by the local shallow crustal structures beneath the stations.

### 3.5. Resolution Test

We tested the reliability of the imaged features through multiple synthetic tests using models with checkerboard and specific patterns. All test processes were conducted under the same settings used in the inversion of real data. For checkerboard models, we assigned checkers with a peak amplitude of  $\pm 0.3$  km/s and size of  $15 \times 15 \times 15$  km (north-south  $\times$  east-west  $\times$  vertical), which is similar to the dimension of the smallest-velocity anomaly obtained in the solution model. Gaussian noise equivalent to the root-mean-square (RMS) of estimated residual uncertainties was added to synthetic  $P$  wave (31 ms) and  $S$  wave (71 ms) traveltimes data. We additionally tested different checkerboard models with the same checker size but different levels of Gaussian noise (twice the RMS error) and with different checker sizes ( $10 \times 10 \times 10$  and  $30 \times 30 \times 30$  km) but the same level of Gaussian noise. For recovery tests with specific patterns, we conducted tomographic inversion with spatially separated spike anomalies and several cases of synthetic velocity structures to assess the reliability of the observed velocity structures. In addition, we tested the tomographic inversion under different conditions, namely, inversion without station terms and inversion with some portions of the original data to assess the consistency of the observed results (see section 4.3 for further details).

## 4. Results

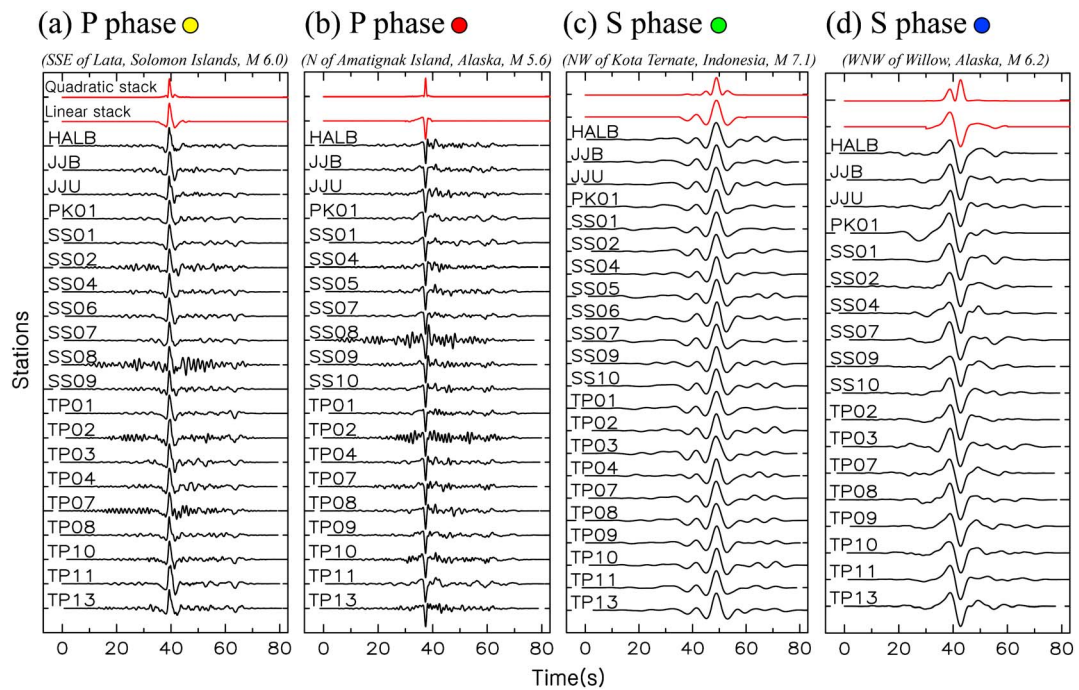
### 4.1. Relative Arrival Time Residual

Figure 3 shows examples of waveforms from the four teleseismic sources shown in Figure 2 that were aligned by the adaptive stacking procedure. The residual maps corresponding to each trace are shown in Figure 4. In general, later arrivals were observed at stations located at greater distances, where raypaths had to pass through the central region of JI. This suggests that relatively slow velocity structures exist beneath the center of the island, which delayed wave propagation. In addition, observed variations in residual patterns implied a certain degree of complexity in velocity structures in the lithosphere beneath JI.

Histograms of the uncertainties for the source examples in Figure 3 are shown in Figure S3. Generally, higher uncertainties were estimated in  $S$  wave than in  $P$  wave residual data because of the longer-period waveforms used for the former. Higher uncertainties obtained at some stations (e.g., stations TP02 and SS08 in Figure S3b and corresponding waveforms in Figure 3b) could be attributed to relatively noisy conditions or incoherent waveforms resulting from local structural heterogeneities (Rawlinson & Kennett, 2004). The RMS of the uncertainties for all observed  $P$  and  $S$  wave data was estimated as 31 and 71 ms, respectively.

### 4.2. Solution Models

The final models obtained by the tomographic inversion process resulted in a reduction of data variance by 34% from  $0.0082$  to  $0.0054$   $s^2$  (from 90.5 to 73.8 ms in RMS) for  $P$  wave tomography (Figure 5a) and by 33% from  $0.0572$  to  $0.0385$   $s^2$  (from 239.2 to 196.1 ms in RMS) for  $S$  wave tomography (Figure 5b). The reduction of data variance was not substantial despite the clear improvement due to unaccounted factors, such as unsolvable small-scale or shallow structures, anisotropy, heterogeneous velocity structures beneath the model space (Rawlinson et al., 2006), or relatively small traveltime variances in the modeled region compared to the noise level.



**Figure 3.** Examples of teleseismic (a and b)  $P$  waveforms and (c and d)  $S$  waveforms recorded by the stations on Jeju Island (JI). Each section of the waveforms was aligned using the adaptive stacking technique (Rawlinson & Kennett, 2004). The two topmost waveforms in red correspond to the quadratic and linear stacks, respectively, and the waveforms in black are signals recorded at given stations (e.g., station HALB). Circles next to the panel titles are coded in the same color as the circles in Figure 2 to indicate the waveform source location.

Depth slices of the 3-D  $P$  wave tomography model from 15 to 55 km (Figure 6) reveal a characteristic pattern of relatively low velocity anomalies beneath the island that varies in shape and location at different depths. At depths of 45 and 55 km (Figures 6c and 6d), a strong low-velocity anomaly ( $<-0.2$  km/s) was observed beneath the central part of the island (Anomaly 1). At a depth of 30 km (Figure 6b), the deeper anomaly divides into narrower low-velocity zones (Anomaly 2). The pattern of low-velocity anomalies becomes more complex at a depth of 15 km (Figure 6a).

We observed relatively high velocities ( $>0.1$  km/s) to the north, east, and west of the island at greater depths (Figure 6d), where a strong contrast exists between the central low-velocity and high-velocity areas. In the vertical profile at 126.50°E (Figure 6f), the high-velocity structure occurs at around 33.6°N, whereas the low-velocity zones are located beneath and to the south of JI. In the east-west vertical profile at 33.35°N (Figure 6e), the high-velocity regions are visible to the east and west of the island.

The results of  $S$  wave tomography are shown in Figure 7. The overall patterns of velocity anomalies are similar to the  $P$  wave structure, showing a low-velocity anomaly at the center of the island while relatively high velocities to the north, east, and west. However, the relatively small scale pattern of the low-velocity anomaly revealed by  $P$  wave tomography was not identified. This loss in resolution may be attributed to one or a combination of factors, such as the longer wavelengths of  $S$  wave signals, higher uncertainties in estimated residuals, and the relatively small number of residual data (Bastow et al., 2008).

#### 4.3. Resolution of Solution Models

The inverted models from synthetic  $P$  and  $S$  wave data for checkerboard patterns with checker sizes of  $15 \times 15 \times 15$  km (Figures 8a–8j) and  $30 \times 30 \times 30$  km (Figures 8k–8r) show generally good horizontal and vertical resolution beneath the island, except for some smearing at the side edges in the vertical slices (e.g., Figures 8g and 8h). The inversion results using a higher level of noise also preserved the input patterns, although the velocity contrast was degraded (Figure S4). The test using the smaller checker size shows a good resolution at shallower depths (7.5–30 km; Figure S5), which indicates that structures as small as 10 km in horizontal scale are resolvable at depths above 30 km.

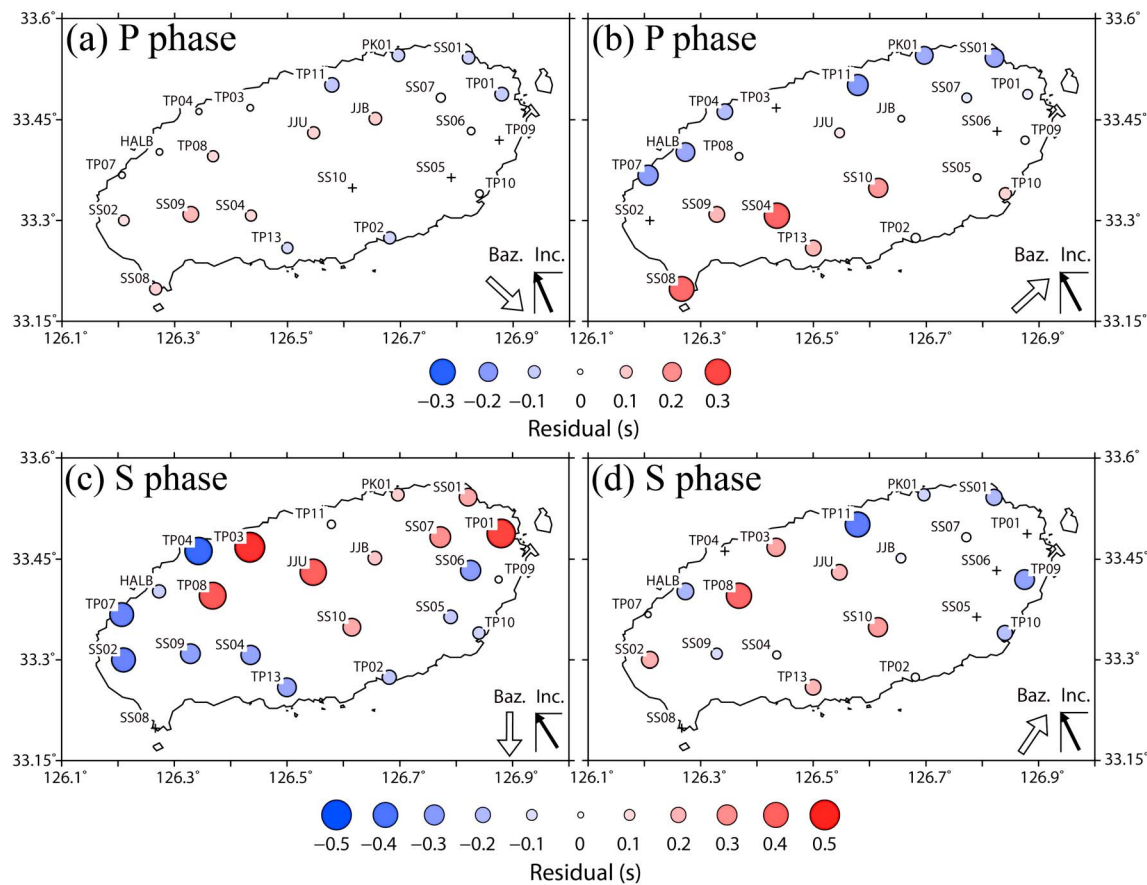


**Figure 4.** Relative arrival time residuals for the four events shown in Figure 2, calculated by adaptive stacking using the traces shown in Figure 3. Maps of  $P$  wave residuals for the traces in (a) Figure 3a and (b) Figure 3b. Maps of  $S$  wave residuals for the traces in (c) Figure 3c and (d) Figure 3d. The value of each residual is indicated by the size and color of the circle. The back azimuth (Baz.) and event incidence angles (Inc.) are denoted by the arrows in the bottom right corner of each map. Stations without arrival time measurements are indicated with a cross.

In addition to the checkerboard tests, we conducted a synthetic test with six spatially distributed spikes (peak amplitude of  $\pm 0.4$  km/s) to check the extent of smearing in different locations and depths. The solution model (Figure S6) successfully recovered all the input anomalies, although vertical smearing appears particularly at greater depths.

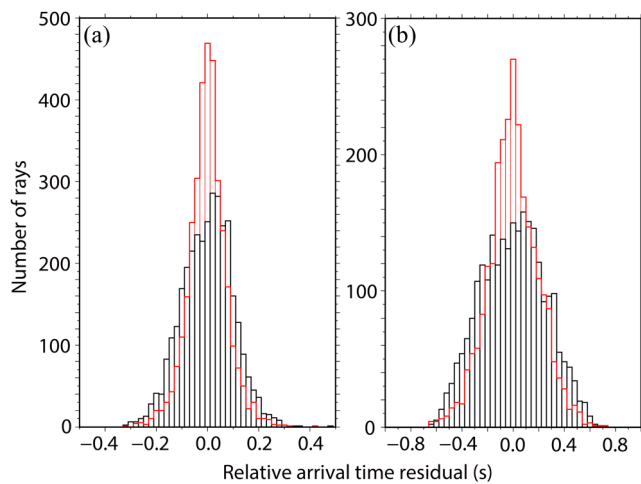


**Figure 5.** Histograms of relative arrival time misfit obtained from initial models (black) and solution models (red) of (a)  $P$  wave and (b)  $S$  wave tomography.

We further conducted recovery tests using the specific patterns (Figures 9, S7, and S8) observed in the  $P$  wave tomography (Figure 6). To investigate the reliability of observed velocity structures at greater depths (Anomaly 1 and surrounding relatively high velocity regions in Figure 6d), we assumed a low-velocity structure located at the center of the island at a depth of 55 km, with a size of  $30 \times 30$  km in the horizontal dimension and height of 15 km (Figure S7a). The input pattern is well constrained without significant horizontal offset or smearing. Interestingly, only weak positive velocities (not exceeding 0.05 km/s) appear around the low-velocity anomaly as inversion artifacts compensating for the input low-velocity anomaly. For comparison, we created a model with the same low-velocity anomaly (Figure S7a) with neighboring higher-velocity structures to the north, east, and west of the island (Figure S7b). Although the size and amplitude of the input anomalies were underestimated, the locations of the positive and negative input structures were effectively resolved. Thus, it is likely that the observed high-velocity structures at greater depths and the low-velocity structure in the center of the island are reliable.

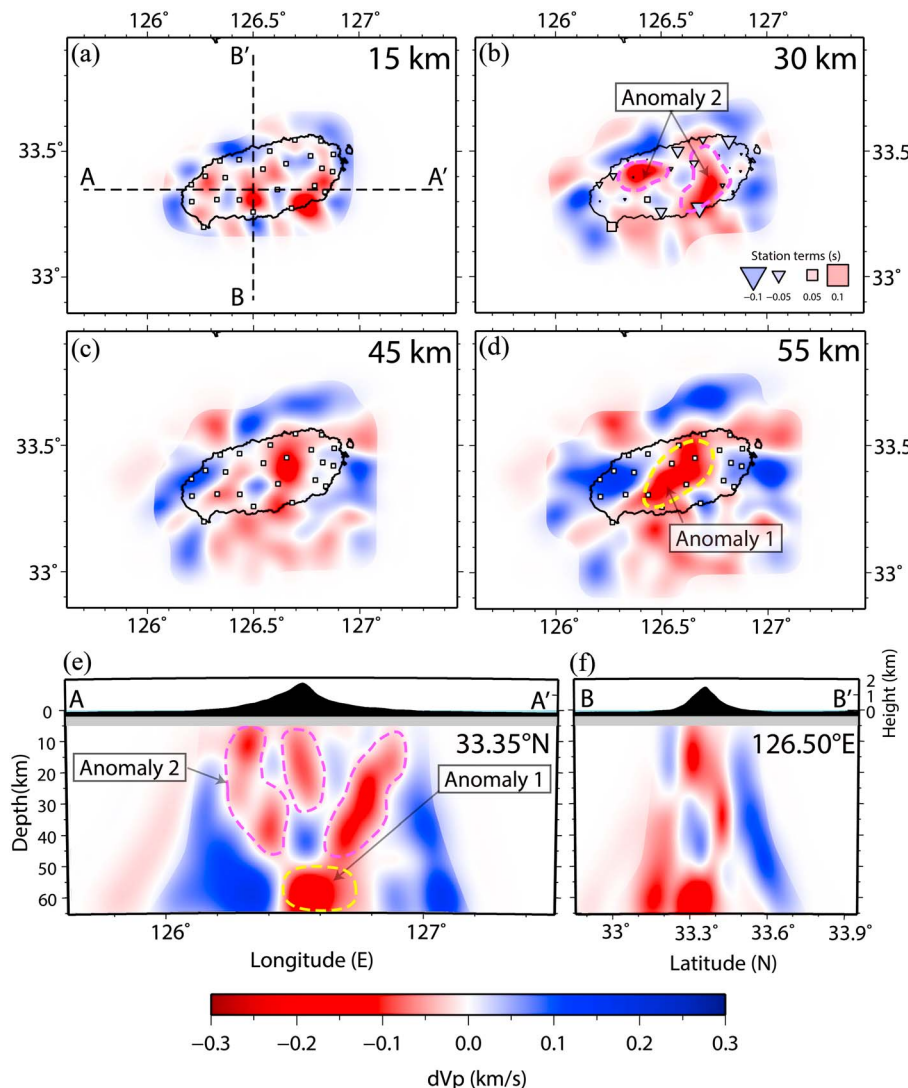


**Figure 6.**  $P$  wave tomography results. (a–d) Depth slices at 15, 30, 45, and 55 km. Seismic stations are denoted by white squares in profiles (a), (c), and (d). Station terms calculated by tomographic inversion are shown in (b). (e and f) Vertical profiles at latitude 33.35°N and longitude 126.50°E. Contour lines indicate major features observable in the model (Anomalies 1 and 2).

To determine whether the upward ramifying low-velocity anomaly (Figure 6e) is resolvable, we performed a synthetic test using a conduit shape model. The model consisted of a single column at a depth range of 45–60 km and three separate columns on top that extend from a depth of 45 km to the surface (Figure S8). The input  $P$  wave velocity perturbation was constant at  $-0.3$  km/s. The inverted model successfully resolved the three separated narrow conduits at shallower depths as well as the single column at greater depths.

Figure 9 shows a model resulting from a recovery test using patterns that combined all the structures. The results confirmed that the resolved individual features (Figures S7 and S8) were equally robust in the combined tomography, without underestimating any of the structures or smearing of the dominant features. Therefore, we conclude that the structures in our tomographic results (Anomalies 1 and 2) are reliable.

Additionally, we tested the  $P$  and  $S$  wave tomography results (Figures 6 and 7) under different conditions: (1) inversion without station terms and (2) inversion using a randomly chosen half and quarter of the data. In the second test, we chose only 20% of the rays from the southeast (back azimuth from 120 to 160°, which account

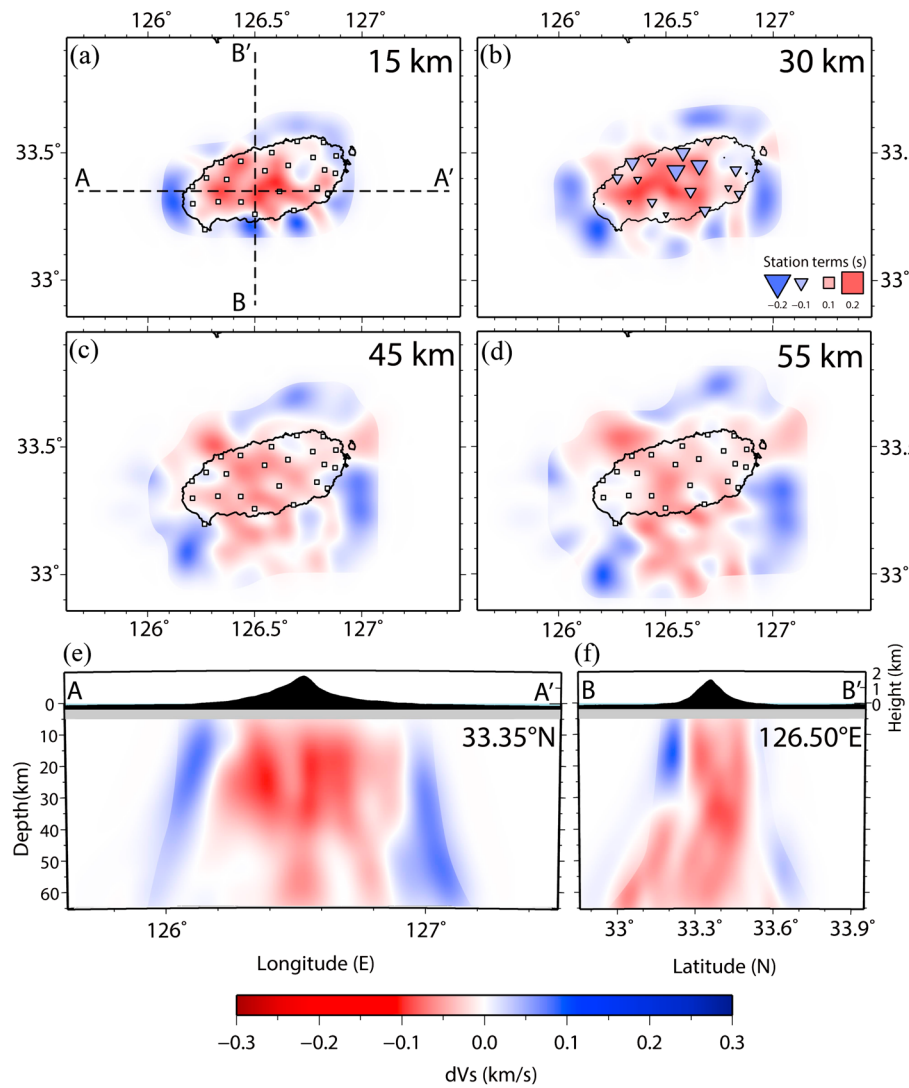


**Figure 7.** *S* wave tomography results. (a–d) Depth slices at 15, 30, 45, and 55 km. Seismic stations are denoted by white squares in profiles (a), (c), and (d). Station terms calculated by tomographic inversion are shown in (b). (e and f) Vertical profiles at latitude 33.35°N and longitude 126.50°E.

for nearly 50% of the original data) to balance the input data. Although we omitted static corrections and some of the original data, the observed structures at depths below 10 km were consistently resolved (Figure S9 and S10).

## 5. Discussion

The main observations from our tomography models are summarized as follows: (1) Relatively low velocity anomalies that extend from the upper crust to the upper mantle (~60 km) exist below the island. (2) The size and pattern of the low-velocity structures vary with depth. A strong low-velocity anomaly was observed beneath the center of the island at greater depths (>50 km, Anomaly 1), while a dispersed low-velocity zone exists at shallower depths (<45 km, Anomaly 2). (3) Relatively high velocity structures exist to the north, east, and west of the central low-velocity zone at greater depths. We used our observations to understand the magmatic structures in the lithosphere beneath Jl. In the following sections, we compare our results with those of previous studies and discuss the possible volcanic systems and mechanisms of the intraplate volcanism in Jl.

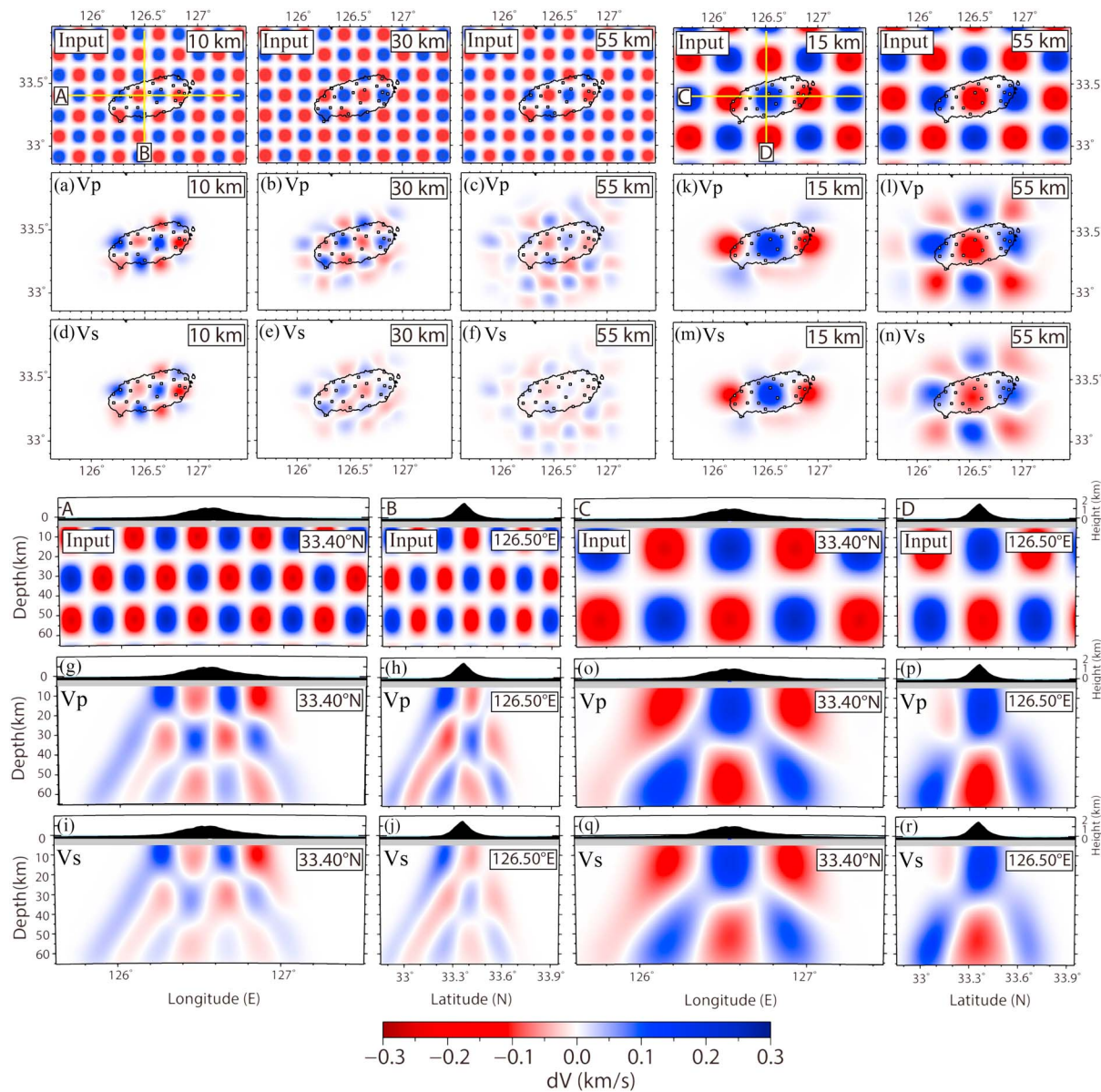


**Figure 8.** Checkerboard test results of  $P$  and  $S$  wave tomography. (a–j) Output models with checker size of  $15 \times 15 \times 15$  km. (k–r) Output models with checker size of  $30 \times 30 \times 30$  km. (a–c) Output models at depths of 10, 30, and 55 km for  $P$  wave tomography. (d–f) Output models at depths of 10, 30, and 55 km for  $S$  wave tomography. (g and h) Output models at latitude  $33.40^{\circ}$ N and longitude  $126.50^{\circ}$ E for  $P$  wave tomography. (i and j) Output models at latitude  $33.40^{\circ}$ N and longitude  $126.50^{\circ}$ E for  $S$  wave tomography. (k and l) Output models at depths of 15 and 55 km for  $P$  wave tomography. (m and n) Output models at depths of 15 and 55 km for  $S$  wave tomography. (o and p) Output models at latitude  $33.40^{\circ}$ N and longitude  $126.50^{\circ}$ E for  $P$  wave tomography. (q and r) Output models at latitude  $33.40^{\circ}$ N and longitude  $126.50^{\circ}$ E for  $S$  wave tomography. Gaussian random noise equivalent to estimated residual error has been imposed on the synthetic data set.

### 5.1. Comparison With Previous Tomographic Studies

In relative traveltime tomography, care should be taken when interpreting images with velocity perturbations because this method only provides relative velocity; absolute velocities are unknown (Aki et al., 1977; Lévéque & Masson, 1999; Rawlinson et al., 2006). Therefore, it is useful to compare previous results that constrain either the velocity structure at larger scales (e.g., global or regional tomography) or the absolute velocity structures, such as when surface wave dispersion data were used (Bastow, 2012).

In global tomography models (Mégnin & Romanowicz, 2000; Ritsema et al., 2011), NE Asia, including JI and the Korean Peninsula, has a relatively slow upper mantle  $S$  wave velocity ( $<-1\%$  at a depth of  $\sim 100$  km). Studies of regional  $P$  wave tomography that cover the East Asia upper mantle (C. Li & Van Der Hilst, 2010;

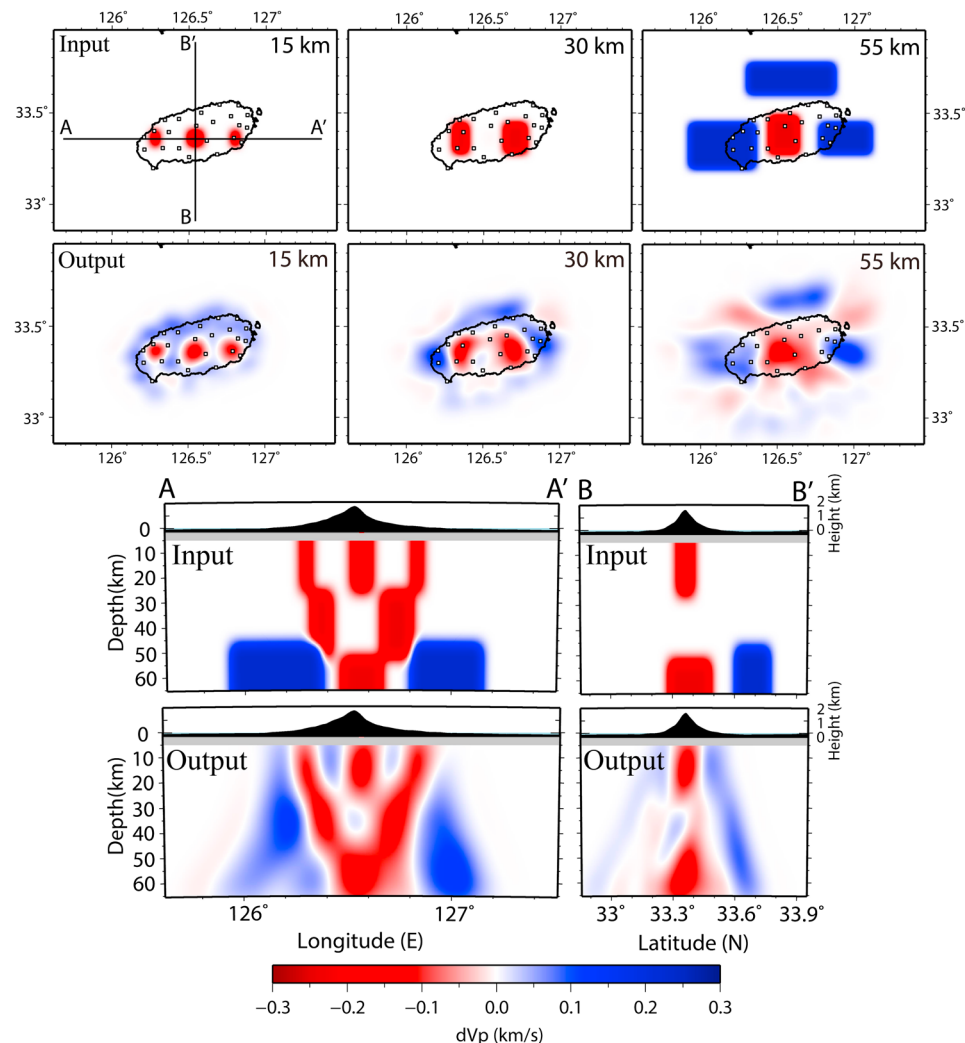


**Figure 9.** Resolution test of  $P$  wave tomography with synthetic velocity structures consisting of the main features in observed results (Figure 6).

W. Wei et al., 2012) also show relatively low velocity anomalies ( $<-1\%$ ) at depths of 50–150 km under JI and the nearest regions. Studies using multimode surface waveform tomography (e.g., Legendre et al., 2015; Pandey et al., 2014; Priestley et al., 2006) have revealed prominent slow  $S$  wave speeds ( $<-2.5\%$ ) at the back-arc basins of the western Pacific subduction zones comprising the East Sea and extending to the East China Sea. These results point to slower upper mantle velocities beneath JI and nearby regions ( $dV_p = -1\%$  and  $dV_s = -1\%$  in lower bounds) compared with the normal mantle velocity. Consequently, we suggest that the low velocity ( $P$  wave velocity  $<-0.15$  km/s) beneath the center of JI observed in our study is potentially slower than the regionally slow upper mantle.

As we showed through the synthetic recovery test (Figures 9 and Figure S7), the higher-velocity structures at greater depths are nontrivial. These structures correspond to the high-velocity anomalies imaged in previous tomographic studies. Global models observed relatively thick lithospheric structures ( $>60$  km) in the central and western parts of the Korean Peninsula (e.g., Pasquano et al., 2014). In regional studies, relatively high velocity anomalies have been consistently observed at locations similar to the regions with relatively thick lithosphere (e.g., Chen et al., 2017; S. Kim et al., 2016; Ma et al., 2018; W. Wei et al., 2012; Zheng et al., 2011). S. Kim et al. (2016) suggest that sharp boundaries of high-to-low-velocity transition exist near JI, which they interpreted to be the lateral boundary at a shallow upper mantle depth ( $<60$  km) between the relatively thick continental lithosphere beneath the Korean Peninsula and East China and the asthenospheric upper mantle beneath regions with a thinner lithosphere.

From our results, the peak-to-peak variation between Anomaly 1 and surrounding high-velocity regions is approximately 0.4 km/s, which corresponds to a 5% velocity perturbation. Considering the globally slow upper mantle in our study area, the velocity reduction of Anomaly 1 could reach 6% in comparison with the normal mantle. However, such large variation is unlikely to form within the sublithospheric mantle beneath the island, compared with active magmatic rift zones or hot spots where a similar magnitude of velocity reduction has been reported in the upper mantle (e.g., Bastow et al., 2008; H.-H. Huang et al., 2015). Considering previously suggested lithospheric structures and the velocity pattern obtained in our study, we suggest that the high-velocity structures represent the southern margin of the lithospheric structures that extended from the Korean Peninsula and East China.

## 5.2. Volcanic System of JI

It has been suggested that the source depth of the magma of JI volcanism should be greater than lithospheric depths to form such a large-volume central shield volcano (Brenna, Cronin, Smith, Maas, & Sohn, 2012) and to explain the geochemical evidence (Baek et al., 2014; Choi et al., 2006). Our image (Figure 6d) shows at least a 0.3-km/s perturbation of *P* wave velocity between the central low-velocity structure (Anomaly 1) and the surrounding high-velocity regions, which is about a 3.7% velocity perturbation with respect to the reference model. Such an observed velocity change corresponds to a temperature variation range of 185–740 °C (Bastow et al., 2005; Goes et al., 2000), considering only the thermal effect on seismic velocity perturbation. It is unlikely for such a large temperature variation to occur within the small area ( $\sim 100 \times 100$  km) without localized melt focusing (e.g., C. Lee & Lim, 2014; Tang et al., 2014). Because the imaged low-velocity features are not localized around JI but cover the entire region of the East China Sea (e.g., W. Wei et al., 2012; Zheng et al., 2011) or extend along the expected margins of the continental lithosphere (e.g., S. Kim et al., 2016), other factors are needed to explain the focused large velocity contrast. It has been suggested that a small fraction (~1–2%) of partial melting (Hammond & Humphreys, 2000; Mavko, 1980; Sobolev et al., 1996) can result in a large velocity contrast in a confined area. Anisotropy can also play a role in the variation of seismic velocity (Gao et al., 2004). However, only a weak (<1.5%) azimuthal anisotropy is suggested beneath JI without abrupt changes in the fast direction and amount of anisotropy (Z. Huang et al., 2004; Kang & Shin, 2009; W. Wei et al., 2016). Compositions and grain sizes of materials in the lithospheric upper mantle may affect seismic velocity (Cammarano et al., 2003; Faul & Jackson, 2005), but they are second-order effects compared to temperature in the upper mantle (Goes et al., 2000). Therefore, it can be argued that Anomaly 1 in our result is a high-temperature upper mantle structure potentially with partial melts (Figure 6).

Small-scale low-velocity perturbations at shallow depths (Anomaly 2) indicate the existence of more complex magmatic structures at lithospheric depths. JI comprises more than 300 small volcanoes (Figure 1c) characterized by geochemical features that favor monogenetic eruptions fed by dispersed and independent plumbing systems (Brenna et al., 2011; G. W. Koh et al., 2013; Sohn et al., 2012). The pattern with narrower low-velocity anomalies depict magmatic paths in the lithosphere that connect the locally ponded melts at sublithospheric depth (Anomaly 1) to the dispersed volcanoes at the surface ( $\sim 100$  km in horizontal scale). The low-velocity structures mainly extend to the east and west of the center of JI. Small-scale volcanoes characterized by more recent basaltic eruptions populate the surface above these low-velocity zones. In addition, the shallow anomalies spatially overlap with central volcanism with a later (~25 ka) large volume of trachyte magma (Brenna, Cronin, Smith, Sohn, & Maas, 2012; Ko & Yun, 2016). Thus, it can be inferred that these anomalies represent a shallow magma plumbing structure related to volcanism with primitive basaltic and evolved magma. Reactivation of individual vents after longer time breaks (>200 ka) has been reported (Brenna, Németh, et al., 2015). The low-velocity pattern at shallow depths (<45 km in Figure 6) might be due to more complex magmatic structures overlapping with multiple volcanic eruptions. More scattered low-velocity features can be found at a depth of 15 km (Figure 6a), focused at the center, eastern, and western margins of JI. The central low-velocity portion is located beneath the shield volcano, which erupted basaltic lava and formed a trachytic dome. However, the other narrow low-velocity zones are not directly connected to the region with clustered scoria cones (Figure 1c). It is possible that these anomalies were imaged by the smearing of the heterogeneous upper crustal (<10 km) magmatic structures (e.g., narrow sills and dykes) even though the effect of local near-surface structures was taken into account by the station term in inversions. Further investigations are needed to confirm the shallow magmatic structures beneath JI.

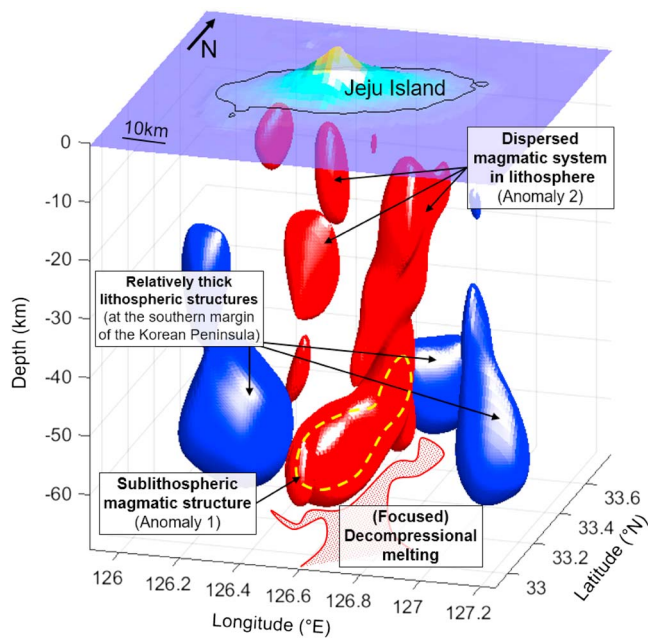


**Figure 10.** Three-dimensional plot of  $P$  wave tomography results with the interpreted main features. Structures in red and blue denote  $-1$  and  $+0.5\%$  velocity isosurfaces, respectively. Yellow dashed line marks the  $-1.5\%$  velocity isosurface at greater depths ( $50$ – $60$  km). Surface topography is vertically exaggerated by five times.

Compared to a magma evolution model based on geochemical data (Brenna, Cronin, Smith, Sohn, & Maas, 2012), our results show similarities in the dispersed magma plumbing system at shallower depths ( $\sim 15$  km) beneath the island, but the seismic images (Figure 6) suggest a more focused origin of the sublithospheric magma.

Our findings of dispersed and complex magmatic structures beneath JI (Figure 6) are suggestive of intensive interaction between the ascending magma and the lithospheric environment (M. Li et al., 2018; Martí et al., 2017; Németh, 2010). Complex magmatic structures within the lithosphere are generally formed by the movement and emplacement of magmas in the lithosphere (e.g., Benz et al., 1996; H.-H. Huang et al., 2015; Martí et al., 2017; Miller & Smith, 1999; Thybo & Artemieva, 2013). Such magma emplacement and movement are controlled by various factors, including local or regional stress fields and preexisting structural (e.g., fault or fracture) or rheological discontinuities (Maccaferri et al., 2010; Martí et al., 2016; Németh, 2010; Takada, 1989; Valentine & Perry, 2007). A previous petrological study on JI revealed that peridotite xenoliths metasomatized by evolved alkali basalt (Yang et al., 2012), which could promote the intensive interaction between the host magma and the lithospheric environment.

### 5.3. Possible Mechanisms of Jeju Intraplate Volcanism

Although previous studies have attempted to explain the mechanism of intraplate volcanism in JI, a consensus has not been reached. Nakamura et al. (1990) and Tatsumi et al. (2005) suggested a possible mantle plume origin. However, the absence of mantle plume signatures, for example,

hot spot tracks, volcanic age progressions, topographic swells, and deep-seated thermal anomalies (Chen et al., 2017; Choi et al., 2006; Y. Kim et al., 2015; Ma et al., 2018), together with the observed nonplume trace element characteristics and relatively low geothermal gradient (Brenna, Cronin, Smith, Maas, & Sohn, 2012), makes the suggestion implausible. Decompressional melting by tectonic extension (Choi et al., 2006) or lithospheric folding (Shin et al., 2012) due to plate interactions have likewise been suggested. However, these simple and large-scale mechanisms cannot explain the focused and isolated volcanism in JI, where neighboring volcanoes aligned to the corresponding stress regime are absent. Localized asthenospheric upwelling can be induced by sublithospheric mantle convections (West et al., 2009). Guo et al. (2018) argued that convective downwelling in the upper mantle beneath the Songliao basin triggered by upwelling beneath the Mt. Baekdu (Changbai) volcano in NE China may have induced localized asthenospheric upwellings in regions surrounding the basin, forming localized and isolated intraplate volcanism. However, no such convective flow has been reported beneath the Korean Peninsula and Yellow Sea, which is coeval with the volcanism in JI despite the proposed tectonic proximity between NE China and the Korean Peninsula, both being part of Sino-Korean old basement with a relatively thick lithosphere (Chough et al., 2000).

Convective mantle flows can be developed by edge-driven convection processes (Conrad et al., 2010; King & Anderson, 1998). Decompressional melting is generated at locations with lithosphere thickness gradients induced by thermal differences or dynamic processes between the relatively thick and thin lithospheres. This mechanism has been used to explain intraplate volcanism without mantle plumes in some regions (Ballmer et al., 2015; Davies & Rawlinson, 2014; S. Kim et al., 2017; King & Ritsema, 2000; Van Wijk et al., 2010, 2008). Based on our results (Figures 6 and 10) and recently improved seismological images of the lithosphere in NE Asia (see section 5.1 for references), JI is located at a transitional region of lithospheric thickness at the southern margin of the continental lithosphere beneath the Korean Peninsula and Yellow Sea. The amount of 3-D heterogeneity in the distribution of high-velocity structures (Figures 6 and 10) may indicate inherent rheological weaknesses or geometrically nonuniform structures along the margin of the thicker lithosphere, which may have been formed during previous extensional events (Chough et al., 2000; Chough & Sohn, 2010). It has been reported that the preexisting structural complexity in the lithosphere controls melt focusing (Davies & Rawlinson, 2014; Davies et al., 2015; Hoke & Lamb, 2007). Hence, it can be

inferred that decompressional melting induced by convective flows at the lithosphere thickness transition could be a possible mechanism of volcanism in JI. To confirm this, further investigation (e.g., geodynamic simulation) is required to demonstrate whether the lithospheric thickness gradient at the continental margin of the Korean Peninsula is sufficient for thermal instability (e.g., Kaislaniemi & Van Hunen, 2014; Missenard & Cadoux, 2012) in the region with low asthenospheric shear (Conrad et al., 2011; King, 2011).

Horizontally and vertically driven mantle flows by a subducting slab could play a role in promoting such decompressional melting at the edge of the continental lithosphere. A subducting slab can trigger 3-D upper mantle flows (Motoki & Ballmer, 2015; Piromallo et al., 2006; Schellart, 2004) and focused upwelling away from the slab (Faccenna et al., 2010). In addition, it has been suggested that the stagnant Pacific slab beneath East Asia induces large-scale convective flows due to deep dehydration (Kameyama & Nishioka, 2012; Richard & Iwamori, 2010; Zhang et al., 2014), which may result in intraplate volcanism (Sakuyama et al., 2013; Wang et al., 2015; Zhao et al., 2009). Furthermore, horizontally induced shear or transported melts are possible based on the extension of the back-arc low-velocity bodies in the Okinawa trough and the Sea of Japan (East Sea) to the continental margin around the Korean Peninsula (S. Kim et al., 2016; Zheng et al., 2011). Such a mechanism has been proposed in back-arc settings (e.g., Brenna, Cronin, et al., 2015; Currie et al., 2008; S. S. Wei et al., 2015).

## 6. Conclusions

By using a dense seismic array consisting of 20 temporary and three permanent stations that were operated for over 2 years and applying teleseismic traveltimes tomography, we obtained detailed 3-D velocity images of the lithospheric structures beneath JI for the first time. We used the adaptive stacking technique to accurately measure the relative arrival time residuals of *P* and *S* wave records. For data inversion and retrieval of velocity structures, we used the fast marching tomography method. A major finding is the identification of a prominent low-velocity anomaly under the summit of the island at greater depths (50–60 km), which separates into narrower low-velocity zones at shallower depths (10–45 km). Moreover, we observed velocity changes from lower velocities beneath the island and southern part of the model space to higher velocities to the north, east, and west of the island at a greater depth (~55 km). Through a series of synthetic recovery tests with checkerboard and specific anomaly patterns, we confirmed that the observed velocity anomalies and patterns are robust and reliable.

Based on previous geological observations, we interpreted the significant low-velocity anomaly (>3.7% reduction in *P* wave velocity compared to surrounding high-velocity structures) beneath the central part of JI at a depth of ~55 km as a sublithospheric high-temperature upper mantle structure potentially with partial melts. The low-velocity anomalies become separated and extend toward the east and west of the island with decreasing depth, and the structure represents a dispersed magmatic system corresponding to the surface features of volcanism in the island. On the other hand, the high-velocity structures to the north, east, and west of the island were interpreted as relatively thick lithospheric structures extending from the southern margin of the lithosphere beneath the Korean Peninsula structure, especially considering that their trend is consistent with a previously observed velocity transition beneath the island and the magnitude of velocity contrast. In summary, we suggest that focused decompressional melting at sublithospheric depths formed at the transition of lithospheric thickness beneath the island, and the intensive interaction between the ascending magma and lithosphere resulted in complex and dispersed intraplate volcanic system in JI.

## References

- Ahn, U. S. (2016). Study of the last volcanic activity on historical records on Jeju Island, Korea. *The Journal of the Petrological Society of Korea*, 25(1), 69–83. <https://doi.org/10.7854/JPSK.2016.25.1.69>
- Ahn, U. S., & Hong, S. S. (2017). Volcanological history of the Baengnokdam summit crater area, Mt. Halla in Jeju Island, Korea. *The Journal of the Petrological Society of Korea*, 26(3), 221–234. <https://doi.org/10.7854/JPSK.2017.26.3.221>
- Aki, K., Christoffersson, A., & Husebye, E. S. (1977). Determination of the three-dimensional seismic structure of the lithosphere. *Journal of Geophysical Research*, 82, 277–296. <https://doi.org/10.1029/JB082i002p00277>
- Argnani, A., Cimini, G. B., Frugoni, F., Monna, S., & Montuori, C. (2016). The role of continental margins in the final stages of arc formation: Constraints from teleseismic tomography of the Gibraltar and Calabrian Arc (Western Mediterranean). *Tectonophysics*, 677–678, 135–152. <https://doi.org/10.1016/j.tecto.2016.03.037>
- Baek, S., Choi, S. H., Lee, S. G., Lee, S. R., & Lee, H. M. (2014). Geochemistry of anorthositic xenolith and host tholeiite basalt from Jeju Island, South Korea. *Geosciences Journal*, 18(2), 125–135. <https://doi.org/10.1007/s12303-013-0060-9>

## Acknowledgments

The authors would like to thank Sang-Jun Lee, Jeong-Ung Woo, Sungwon Cho, and Juhwan Kim of Seoul National University and Jechan Park, Hyun Ho Jang, Minook Kim, ChangHwan Kong, Euna Park, Hyejin Park, and Dabeen Heo of Pukyong National University for their assistance in the field deployment of the temporary seismic network. We also thank Gee-Pyo Kim (Jeju Special Self-Governing Province), Soo-Hyoung Lee, and Kyoochul Ha (KIGAM) for making the said deployment possible. We appreciate the constructive comments and suggestions of Marco Brenna and one anonymous reviewer, which have improved the original version of the manuscript. Data were partly acquired from the KMA and KIGAM. We acknowledge Nicholas Rawlinson for making his code (Fast Marching Teleseismic Tomography and Adaptive Stacking) available. Most of the figures were generated using Generic Mapping Tools (Wessel et al., 2013). Seismic waveform data, velocity models, and traveltimes residuals along with format description are available from <https://doi.org/10.6084/m9.figshare.6149858.v1> (Song et al., 2018). This work was funded by the Korea Meteorological Administration Research and Development Program under grant KMIPA2017-4020.

- Ballmer, M. D., Conrad, C. P., Smith, E. I., & Johnsen, R. (2015). Intraplate volcanism at the edges of the Colorado Plateau sustained by a combination of triggered edge-driven convection and shear-driven upwelling. *Geochemistry, Geophysics, Geosystems*, 16, 366–379. <https://doi.org/10.1002/2014GC005641>
- Bastow, I. D. (2012). Relative arrival-time upper-mantle tomography and the elusive background mean. *Geophysical Journal International*, 190(2), 1271–1278. <https://doi.org/10.1111/j.1365-246X.2012.05559.x>
- Bastow, I. D., Nyblade, A. A., Stuart, G. W., Rooney, T. O., & Benoit, M. H. (2008). Upper mantle seismic structure beneath the Ethiopian hot spot: Rifting at the edge of the African low-velocity anomaly. *Geochemistry, Geophysics, Geosystems*, 9, Q12022. <https://doi.org/10.1029/2008GC002107>
- Bastow, I. D., Stuart, G. W., Kendall, J. M., & Ebinger, C. J. (2005). Upper-mantle seismic structure in a region of incipient continental breakup: Northern Ethiopian rift. *Geophysical Journal International*, 162(2), 479–493. <https://doi.org/10.1111/j.1365-246X.2005.02666.x>
- Benz, H. M., Chouet, B. A., Dawson, P. B., Lahr, J. C., Page, R. A., & Hole, J. A. (1996). Three-dimensional *P* and *S* wave velocity structure of Redoubt Volcano, Alaska. *Journal of Geophysical Research*, 101, 8111–8128. <https://doi.org/10.1029/95JB03046>
- Bird, P. (2003). An updated digital model of plate boundaries. *Geochemistry, Geophysics, Geosystems*, 4(3), 1027. <https://doi.org/10.1029/2001GC000252>
- Biryol, C. B., Beck, S. L., Zandt, G., & Özcar, A. A. (2011). Segmented African lithosphere beneath the Anatolian region inferred from teleseismic *P* wave tomography. *Geophysical Journal International*, 184(3), 1037–1057. <https://doi.org/10.1111/j.1365-246X.2010.04910.x>
- Brenna, M., Cronin, S. J., Keresztsuri, G., Sohn, Y. K., Smith, I. E. M., & Wijbrans, J. (2015). Intraplate volcanism influenced by distal subduction tectonics at Jeju Island, Republic of Korea. *Bulletin of Volcanology*, 77(1), 7. <https://doi.org/10.1007/s00445-014-0896-5>
- Brenna, M., Cronin, S. J., Németh, K., Smith, I. E. M., & Sohn, Y. K. (2011). The influence of magma plumbing complexity on monogenetic eruptions, Jeju Island, Korea. *Terra Nova*, 23(2), 70–75. <https://doi.org/10.1111/j.1365-3121.2010.00985.x>
- Brenna, M., Cronin, S. J., Smith, I. E. M., Maas, R., & Sohn, Y. K. (2012). How small-volume basaltic magmatic systems develop: A case study from the Jeju Island volcanic field, Korea. *Journal of Petrology*, 53(5), 985–1018. <https://doi.org/10.1093/petrology/egs007>
- Brenna, M., Cronin, S. J., Smith, I. E. M., Sohn, Y. K., & Maas, R. (2012). Spatio-temporal evolution of a dispersed magmatic system and its implications for volcano growth, Jeju Island Volcanic Field, Korea. *Lithos*, 148, 337–352. <https://doi.org/10.1016/j.lithos.2012.06.021>
- Brenna, M., Cronin, S. J., Smith, I. E. M., Sohn, Y. K., & Németh, K. (2010). Mechanisms driving polymagmatic activity at a monogenetic volcano, udo, Jeju Island, South Korea. *Contributions to Mineralogy and Petrology*, 160(6), 931–950. <https://doi.org/10.1007/s00410-010-0515-1>
- Brenna, M., Németh, K., Cronin, S. J., Sohn, Y. K., Smith, I. E., & Wijbrans, J. (2015). Co-located monogenetic eruptions~200 kyr apart driven by tapping vertically separated mantle source regions, Chagwido, Jeju Island, Republic of Korea. *Bulletin of Volcanology*, 77(5), 43. <https://doi.org/10.1007/s00445-015-0928-9>
- Cammarano, F., Goes, S., Vacher, P., & Giardini, D. (2003). Inferring upper-mantle temperatures from seismic velocities. *Physics of the Earth and Planetary Interiors*, 138(3–4), 197–222. [https://doi.org/10.1016/S0031-9201\(03\)00156-0](https://doi.org/10.1016/S0031-9201(03)00156-0)
- Cañón-Tapia, E., & Walker, G. P. (2004). Global aspects of volcanism: The perspectives of “plate tectonics” and “volcanic systems”. *Earth-Science Reviews*, 66(1–2), 163–182. <https://doi.org/10.1016/j.earscirev.2003.11.001>
- Chen, C., Zhao, D., Tian, Y., Wu, S., Hasegawa, A., Lei, J., et al. (2017). Mantle transition zone, stagnant slab and intraplate volcanism in Northeast Asia. *Geophysical Journal International*, 209(1), ggw491–ggw485. <https://doi.org/10.1093/gji/ggw491>
- Choi, S. H., Mukasa, S. B., Kwon, S.-T., & Andronikov, A. V. (2006). Sr, Nd, Pb and Hf isotopic compositions of late Cenozoic alkali basalts in South Korea: Evidence for mixing between the two dominant asthenospheric mantle domains beneath East Asia. *Chemical Geology*, 232(3–4), 134–151. <https://doi.org/10.1016/j.chemgeo.2006.02.014>
- Chough, S. K., Kwon, S. T., Ree, J. H., & Choi, D. K. (2000). Tectonic and sedimentary evolution of the Korean Peninsula: A review and new view. *Earth-Science Reviews*, 52(1–3), 175–235. [https://doi.org/10.1016/S0016-8252\(00\)00029-5](https://doi.org/10.1016/S0016-8252(00)00029-5)
- Chough, S. K., & Sohn, Y. K. (2010). Tectonic and sedimentary evolution of a Cretaceous continental arc-backarc system in the Korean Peninsula: New view. *Earth-Science Reviews*, 101(3–4), 225–249. <https://doi.org/10.1016/j.earscirev.2010.05.004>
- Connor, C. B., & Conway, F. M. (2000). Basaltic volcanic fields. In H. Sigurdsson (Ed.), *Encyclopedia of volcanoes*, (pp. 331–343). San Diego, CA: Academic.
- Conrad, C. P., Bianco, T. A., Smith, E. I., & Wessel, P. (2011). Patterns of intraplate volcanism controlled by asthenospheric shear. *Nature Geoscience*, 4(5), 317–321. <https://doi.org/10.1038/ngeo1111>
- Conrad, C. P., Wu, B., Smith, E. I., Bianco, T. A., & Tibbetts, A. (2010). Shear-driven upwelling induced by lateral viscosity variations and asthenospheric shear: A mechanism for intraplate volcanism. *Physics of the Earth and Planetary Interiors*, 178(3–4), 162–175. <https://doi.org/10.1016/j.pepi.2009.10.001>
- Currie, C. A., Huismans, R. S., & Beaumont, C. (2008). Thinning of continental backarc lithosphere by flow-induced gravitational instability. *Earth and Planetary Science Letters*, 269(3–4), 436–447. <https://doi.org/10.1016/j.epsl.2008.02.037>
- Davies, D. R., & Rawlinson, N. (2014). On the origin of recent intraplate volcanism in Australia. *Geology*, 42(12), 1031–1034. <https://doi.org/10.1130/G36093.1>
- Davies, D. R., Rawlinson, N., Iaffaldano, G., & Campbell, I. H. (2015). Lithospheric controls on magma composition along Earth’s longest continental hotspot track. *Nature*, 525(7570), 511–514. <https://doi.org/10.1038/nature14903>
- Faccenna, C., Becker, T. W., Lallemand, S., Lagabrielle, Y., Funiciello, F., & Piromallo, C. (2010). Subduction-triggered magmatic pulses: A new class of plumes? *Earth and Planetary Science Letters*, 299(1–2), 54–68. <https://doi.org/10.1016/j.epsl.2010.08.012>
- Faul, U. H., & Jackson, I. (2005). The seismological signature of temperature and grain size variations in the upper mantle. *Earth and Planetary Science Letters*, 234(1–2), 119–134. <https://doi.org/10.1016/j.epsl.2005.02.008>
- Gao, W., Grand, S. P., Baldridge, W. S., Wilson, D., West, M., Ni, J. F., & Aster, R. (2004). Upper mantle convection beneath the central Rio Grande rift imaged by *P* and *S* wave tomography. *Journal of Geophysical Research*, 109, B03305. <https://doi.org/10.1029/2003JB002743>
- Goes, S., Govers, R., & Vacher, P. (2000). Shallow mantle temperatures under Europe from *P* and *S* wave tomography. *Journal of Geophysical Research*, 105, 11,153–11,169. <https://doi.org/10.1029/1999JB900300>
- Guo, Z., Wang, K., Yang, Y., Tang, Y., John Chen, Y., & Hung, S. H. (2018). The origin and mantle dynamics of Quaternary intraplate volcanism in Northeast China from joint inversion of surface wave and body wave. *Journal of Geophysical Research*, 123, 2410–2425. <https://doi.org/10.1002/2017JB014948>
- Hammond, W. C., & Humphreys, E. D. (2000). Upper mantle seismic wave velocity: Effects of realistic partial melt geometries. *Journal of Geophysical Research*, 105, 10,975–10,986. <https://doi.org/10.1029/2000JB900041>
- Hoernle, K., White, J. D. L., Van den Boogaard, P., Hauff, F., Coombs, D. S., Werner, R., et al. (2006). Cenozoic intraplate volcanism on New Zealand: Upwelling induced by lithospheric removal. *Earth and Planetary Science Letters*, 248(1–2), 350–367. <https://doi.org/10.1016/j.epsl.2006.06.001>

- Hoke, L., & Lamb, S. (2007). Cenozoic behind-arc volcanism in the Bolivian Andes, South America: Implications for mantle melt generation and lithospheric structure. *Journal of the Geological Society*, 164(4), 795–814. <https://doi.org/10.1144/0016-76492006-092>
- Huang, H.-H., Lin, F.-C., Schmandt, B., Farrell, J., Smith, R. B., & Tsai, V. C. (2015). The Yellowstone magmatic system from the mantle plume to the upper crust. *Science*, 348(6236), 773–776. <https://doi.org/10.1126/science.aaa5648>
- Huang, Z., Peng, Y., Luo, Y., Zheng, Y., & Su, W. (2004). Azimuthal anisotropy of Rayleigh waves in East Asia. *Geophysical Research Letters*, 31, L15617. <https://doi.org/10.1029/2004GL020399>
- Iwasaki, T., Sato, H., Ishiyama, T., Shinohara, M., & Hashima, A. (2015). Fundamental Structure Model of Island Arcs and Subducted Plates in and around Japan. Paper presented at the American Geophysical Union Fall Meeting.
- Kaislaniemi, L., & Van Hunen, J. (2014). Dynamics of lithospheric thinning and mantle melting by edge-driven convection: Application to Moroccan Atlas mountains. *Geochemistry, Geophysics, Geosystems*, 15, 3175–3189. <https://doi.org/10.1002/2014GC005414>
- Kameyama, M., & Nishioka, R. (2012). Generation of ascending flows in the big mantle wedge (BMW) beneath Northeast Asia induced by retreat and stagnation of subducted slab. *Geophysical Research Letters*, 39, L10309. <https://doi.org/10.1029/2012GL051678>
- Kang, T.-S., & Shin, J. S. (2009). Shear-wave splitting beneath southern Korea and its tectonic implication. *Tectonophysics*, 471(3-4), 232–239. <https://doi.org/10.1016/j.tecto.2009.02.021>
- Kennett, B. L. N., Engdahl, E. R., & Buland, R. (1995). Constraints on seismic velocities in the Earth from traveltimes. *Geophysical Journal International*, 122(1), 108–124. <https://doi.org/10.1111/j.1365-246X.1995.tb03540.x>
- Kennett, B. L. N., Cambridge, M. S., & Williamson, P. R. (1988). Subspace methods for large inverse problems with multiple parameter classes. *Geophysical Journal International*, 94(2), 237–247. <https://doi.org/10.1111/j.1365-246X.1988.tb05898.x>
- Kim, K. H., Tanaka, T., Suzuki, K., Nagao, K., & Park, E. J. (2002). Evidences of the presence of old continental basement in Cheju volcanic Island, South Korea, revealed by radiometric ages and Nd-Sr isotopes of granitic rocks. *Geochemical Journal*, 36(5), 421–441. <https://doi.org/10.2343/geochim.36.421>
- Kim, S., Tkalcic, H., & Rhee, J. (2017). Seismic constraints on magma evolution beneath Mount Baekdu (Changbai) volcano from transdimensional Bayesian inversion of ambient noise data. *Journal of Geophysical Research: Solid Earth*, 122, 5452–5473. <https://doi.org/10.1002/2017JB014105>
- Kim, S., Tkalcic, H., Rhee, J., & Chen, Y. (2016). Intraplate volcanism controlled by back-arc and continental structures in NE Asia inferred from transdimensional Bayesian ambient noise tomography. *Geophysical Research Letters*, 43, 8390–8398. <https://doi.org/10.1002/2016GL069483>
- Kim, Y., Lee, C., & Kim, S. S. (2015). Tectonics and volcanism in East Asia: Insights from geophysical observations. *Journal of Asian Earth Sciences*, 113(2), 842–856. <https://doi.org/10.1016/j.jseas.2015.07.032>
- King, S. D. (2011). Eruptions above mantle shear. *Nature Geoscience*, 4(5), 279–280. <https://doi.org/10.1038/ngeo1135>
- King, S. D., & Anderson, D. L. (1998). Edge-driven convection. *Earth and Planetary Science Letters*, 160(3-4), 289–296. [https://doi.org/10.1016/S0012-821X\(98\)00089-2](https://doi.org/10.1016/S0012-821X(98)00089-2)
- King, S. D., & Ritsema, J. (2000). African hot spot volcanism: Small-scale convection in the upper mantle beneath cratons. *Science*, 290(5494), 1137–1140. <https://doi.org/10.1126/science.290.5494.1137>
- Ko, B. K., & Yun, S. H. (2016). A preliminary study on calculating eruption volumes of monogenetic volcanoes and volcanic hazard evaluation in Jeju Island. *Journal of Petrological Society of Korea*, 25(2), 143–149. <https://doi.org/10.7854/JPSK.2016.25.2.143>
- Koh, G. W., Park, J. B., Kang, B.-R., Kim, G.-P., & Moon, D. C. (2013). Volcanism in Jeju Island. *Journal of the Geological Society of Korea*, 49(2), 209–230. <https://doi.org/10.14770/jgsk.2013.49.2.209>
- Koh, J. S., Yun, S. H., & Kang, S. S. (2003). Petrology of the volcanic rocks in the Paekrogdam crater area, Mt. Halla, Jeju Island. *Journal of the Geological Society of Korea*, 12(1), 1–15.
- Le Corvec, N., Spörl, K. B., Rowland, J., & Lindsay, J. (2013). Spatial distribution and alignments of volcanic centers: Clues to the formation of monogenetic volcanic fields. *Earth-Science Reviews*, 124, 96–114. <https://doi.org/10.1016/j.earscirev.2013.05.005>
- Lee, C., & Lim, C. (2014). Short-term and localized plume-slab interaction explains the genesis of Abukuma adakite in northeastern Japan. *Earth and Planetary Science Letters*, 396, 116–124. <https://doi.org/10.1016/j.epsl.2014.04.009>
- Lee, M. W. (1982). Petrology and geochemistry of Jeju volcanic island, Korea. *Science Report of the Tohoku University, Sendai*, 15(2), 177–256.
- Legendre, C. P., Zhao, L., & Chen, Q. F. (2015). Upper-mantle shear-wave structure under east and Southeast Asia from automated multimode inversion of waveforms. *Geophysical Journal International*, 203(1), 707–719. <https://doi.org/10.1093/gji/ggv322>
- Lei, J., & Zhao, D. (2005). P wave tomography and origin of the Changbai intraplate volcano in Northeast Asia. *Tectonophysics*, 397(3–4), 281–295. <https://doi.org/10.1016/j.tecto.2004.12.009>
- Lévéque, J.-J., & Masson, F. (1999). From ACH tomographic models to absolute velocity models. *Geophysical Journal International*, 137(3), 621–629. <https://doi.org/10.1046/j.1365-246x.1999.00808.x>
- Li, C., & Van Der Hilst, R. D. (2010). Structure of the upper mantle and transition zone beneath Southeast Asia from travelttime tomography. *Journal of Geophysical Research*, 115, B07308. <https://doi.org/10.1029/2009JB006882>
- Li, M., Zhang, S., & Wu, T. (2018). Fine crustal and uppermost mantle S wave velocity structure beneath the Tengchong volcanic area inferred from receiver function and surface-wave dispersion: Constraints on magma chamber distribution. *Bulletin of Volcanology*, 80(3), 25. <https://doi.org/10.1007/s00445-018-1197-1>
- Ma, J., Tian, Y., Liu, C., Zhao, D., Feng, X., & Zhu, H. (2018). P wave tomography of Northeast Asia: Constraints on the western Pacific plate subduction and mantle dynamics. *Physics of the Earth and Planetary Interiors*, 274, 105–126. <https://doi.org/10.1016/j.pepi.2017.11.003>
- Maccaferri, F., Bonafede, M., & Rivalta, E. (2010). A numerical model of dyke propagation in layered elastic media. *Geophysical Journal International*, 180(3), 1107–1123. <https://doi.org/10.1111/j.1365-246X.2009.04495.x>
- Martí, J., López, C., Bartolini, S., Becerril, L., & Geyer, A. (2016). Stress controls of monogenetic volcanism: A review. *Frontiers in Earth Science*, 4, 106. <https://doi.org/10.3389/feart.2016.00106>
- Martí, J., Villaseñor, A., Geyer, A., López, C., & Tryggvason, A. (2017). Stress barriers controlling lateral migration of magma revealed by seismic tomography. *Scientific Reports*, 7(1), 40,757. <https://doi.org/10.1038/srep40757>
- Mavko, G. M. (1980). Velocity and attenuation in partially molten rocks. *Journal of Geophysical Research*, 85, 5173–5189. <https://doi.org/10.1029/JB085iB10p05173>
- Mégnin, C., & Romanowicz, B. (2000). The three-dimensional shear velocity structure of the mantle from the inversion of body, surface and higher-mode waveforms. *Geophysical Journal International*, 143(3), 709–728. <https://doi.org/10.1046/j.1365-246X.2000.00298.x>
- Miller, D. S., & Smith, R. B. (1999). P and S velocity structure of the Yellowstone volcanic field from local earthquake and controlled-source tomography. *Journal of Geophysical Research*, 104, 15,105–15,121. <https://doi.org/10.1029/1998JB900095>
- Missenard, Y., & Cadoux, A. (2012). Can Moroccan Atlas lithospheric thinning and volcanism be induced by edge-driven convection? *Terra Nova*, 24(1), 27–33. <https://doi.org/10.1111/j.1365-3121.2011.01033.x>

- Motoki, M. H., & Ballmer, M. D. (2015). Intraplate volcanism due to convective instability of stagnant slabs in the mantle transition zone. *Geochemistry, Geophysics, Geosystems*, 16, 538–551. <https://doi.org/10.1002/2014GC005608>
- Nakamura, E., Campbell, I. H., McCulloch, M. T., & Sun, S. S. (1989). Chemical geodynamics in a back arc region around the Sea of Japan: Implications for the genesis of alkaline basalts in Japan, Korea, and China. *Journal of Geophysical Research*, 94, 4634–4654. <https://doi.org/10.1029/JB094iB04p04634>
- Nakamura, E., McCulloch, M. T., & Campbell, I. H. (1990). Chemical geodynamics in the back-arc region of Japan based on the trace element and Sr-Nd isotopic compositions. *Tectonophysics*, 174(3-4), 207–233. [https://doi.org/10.1016/0040-1951\(90\)90323-Z](https://doi.org/10.1016/0040-1951(90)90323-Z)
- Németh, K. (2010). Monogenetic volcanic fields: Origin, sedimentary record, and relationship with polygenetic volcanism. In E. Cañón-Tapia, & A. Szakács (Eds.), *What is a volcano?*, (pp. 43–66). Boulder, CO: Geological Society of America. [https://doi.org/10.1130/2010.2470\(04\)2131-2146](https://doi.org/10.1130/2010.2470(04)2131-2146)
- Németh, K., & Keresztri, G. (2015). Monogenetic volcanism: Personal views and discussion. *International Journal of Earth Sciences*, 104(8), 2131–2146. <https://doi.org/10.1007/s00531-015-1243-6>
- Otofuji, Y.-I., Matsuda, T., & Nohda, S. (1985). Opening mode of the Japan Sea inferred from the palaeomagnetism of the Japan Arc. *Nature*, 317(6038), 603–604. <https://doi.org/10.1038/317603a0>
- Pandey, S., Yuan, X., Debayle, E., Priestley, K., Kind, R., Tilman, F., & Li, X. (2014). A 3D shear-wave velocity model of the upper mantle beneath China and the surrounding areas. *Tectonophysics*, 633, 193–210. <https://doi.org/10.1016/j.tecto.2014.07.011>
- Park, K. H., Park, J. B., Cheong, C. S., & Oh, C. W. (2005). Sr, Nd and Pb isotopic systematics of the Cenozoic basalts of the Korean Peninsula and their implications for the Permo-Triassic continental collision boundary. *Gondwana Research*, 8(4), 529–538. [https://doi.org/10.1016/S1342-937X\(05\)71153-9](https://doi.org/10.1016/S1342-937X(05)71153-9)
- Pasyanos, M. E., Masters, T. G., Laske, G., & Ma, Z. (2014). LITHO1.0: An updated crust and lithospheric model of the Earth. *Journal of Geophysical Research: Solid Earth*, 119, 2153–2173. <https://doi.org/10.1002/2013JB010626>
- Piromallo, C., Becker, T. W., Funiciello, F., & Faccenna, C. (2006). Three-dimensional instantaneous mantle flow induced by subduction. *Geophysical Research Letters*, 33, L08304. <https://doi.org/10.1029/2005GL025390>
- Priestley, K., Debayle, E., McKenzie, D., & Plidou, S. (2006). Upper mantle structure of eastern Asia from multimode surface waveform tomography. *Journal of Geophysical Research*, 111, B10304. <https://doi.org/10.1029/2005JB004082>
- Rawlinson, N., & Kennett, B. L. N. (2004). Rapid estimation of relative and absolute delay times across a network by adaptive stacking. *Geophysical Journal International*, 157(1), 332–340. <https://doi.org/10.1111/j.1365-246X.2004.02188.x>
- Rawlinson, N., & Kennett, B. L. N. (2008). Teleseismic tomography of the upper mantle beneath the southern Lachlan Orogen, Australia. *Physics of the Earth and Planetary Interiors*, 167(1–2), 84–97. <https://doi.org/10.1016/j.pepi.2008.02.007>
- Rawlinson, N., Reading, A. M., & Kennett, B. L. N. (2006). Lithospheric structure of Tasmania from a novel form of teleseismic tomography. *Journal of Geophysical Research*, 111, B02301. <https://doi.org/10.1029/2005JB003803>
- Rawlinson, N., & Sambridge, M. (2004). Wave front evolution in strongly heterogeneous layered media using the fast marching method. *Geophysical Journal International*, 156(3), 631–647. <https://doi.org/10.1111/j.1365-246X.2004.02153.x>
- Richard, G. C., & Iwamori, H. (2010). Stagnant slab, wet plumes and Cenozoic volcanism in East Asia. *Physics of the Earth and Planetary Interiors*, 183(1–2), 280–287. <https://doi.org/10.1016/j.pepi.2010.02.009>
- Ritsema, J., Deuss, A., Van Heijst, H. J., & Woodhouse, J. H. (2011). S40RTS: A degree-40 shear-velocity model for the mantle from new Rayleigh wave dispersion, teleseismic traveltime and normal-mode splitting function measurements. *Geophysical Journal International*, 184(3), 1223–1236. <https://doi.org/10.1111/j.1365-246X.2010.04884.x>
- Sager, W. W., Handschuhmacher, D. W., Hilde, T. W., & Bracey, D. R. (1988). Tectonic evolution of the northern Pacific plate and Pacific-Farallon Izanagi triple junction in the Late Jurassic and Early Cretaceous (M21–M10). *Tectonophysics*, 155(1–4), 345–364. [https://doi.org/10.1016/0040-1951\(88\)90274-0](https://doi.org/10.1016/0040-1951(88)90274-0)
- Sakuyama, T., Tian, W., Kimura, J. I., Fukao, Y., Hirahara, Y., Takahashi, T., et al. (2013). Melting of dehydrated oceanic crust from the stagnant slab and of the hydrated mantle transition zone: Constraints from Cenozoic alkaline basalts in eastern China. *Chemical Geology*, 359, 32–48. <https://doi.org/10.1016/j.chemgeo.2013.09.012>
- Schellart, W. P. (2004). Kinematics of subduction and subduction-induced flow in the upper mantle. *Journal of Geophysical Research*, 109, B07401. <https://doi.org/10.1029/2004JB002970>
- Schlömer, A., Geissler, W. H., Jokat, W., & Jegen, M. (2017). Hunting for the Tristan mantle plume—An upper mantle tomography around the volcanic island of Tristan da Cunha. *Earth and Planetary Science Letters*, 462, 122–131. <https://doi.org/10.1016/j.epsl.2016.12.028>
- Schmandt, B., & Lin, F.-C. (2014). P and S wave tomography of the mantle beneath the United States. *Geophysical Research Letters*, 41, 6342–6349. <https://doi.org/10.1002/2014GL061231>
- Shin, Y. H., Choi, K. S., Koh, J.-S., Yun, S.-H., Nakamura, E., & Na, S.-H. (2012). Lithospheric-folding-based understanding on the origin of the back-arc basaltic magmatism beneath Jeju volcanic island. *Tectonics*, 31, TC4005. <https://doi.org/10.1029/2011TC003092>
- Smith, I. E. M., & Németh, K. (2017). Source to surface model of monogenetic volcanism: A critical review. *Geological Society, London, Special Publications*, 446(1), 1–28. <https://doi.org/10.1144/sp446.14>
- Sobolev, S. V., Zeyen, H., Stoll, G., Werling, F., Altherr, R., & Fuchs, K. (1996). Upper mantle temperatures from teleseismic tomography of French Massif Central including effects of composition, mineral reactions, anharmonicity, anelasticity, and partial melt. *Earth and Planetary Science Letters*, 139(1–2), 147–163. [https://doi.org/10.1016/0012-821X\(95\)00238-8](https://doi.org/10.1016/0012-821X(95)00238-8)
- Sohn, Y. K., Cronin, S. J., Brenna, M., Smith, I. E. M., Németh, K., White, J. D. L., et al. (2012). Ilchulbong tuff cone, Jeju Island, Korea, revisited: A compound monogenetic volcano involving multiple magma pulses, shifting vents, and discrete eruptive phases. *GSA Bulletin*, 124(3–4), 259–274. <https://doi.org/10.1130/B30447.1>
- Sohn, Y. K., & Park, K. H. (2004). Early-stage volcanism and sedimentation of Jeju Island revealed by the Sagye borehole, SW Jeju Island, Korea. *Geosciences Journal*, 8(1), 73–84. <https://doi.org/10.1007/bf02910280>
- Sohn, Y. K., & Park, K. H. (2005). Composite tuff ring/cone complexes in Jeju Island, Korea: Possible consequences of substrate collapse and vent migration. *Journal of Volcanology and Geothermal Research*, 141(1–2), 157–175. <https://doi.org/10.1016/j.jvolgeores.2004.10.003>
- Sohn, Y. K., Park, K. H., & Yoon, S.-H. (2008). Primary versus secondary and subaerial versus submarine hydrovolcanic deposits in the sub-surface of Jeju Island, Korea. *Sedimentology*, 55(4), 899–924. <https://doi.org/10.1111/j.1365-3091.2007.00927.x>
- Sohn, Y. K., Yoon, W. S., Ahn, U. S., Kim, G. B., Lee, J. H., Ryu, C. K., et al. (2015). Stratigraphy and age of the human footprints-bearing strata in Jeju Island, Korea: Controversies and new findings. *Journal of Archaeological Science: Reports*, 4, 264–275. <https://doi.org/10.1016/j.jasrep.2015.09.014>
- Song, J.-H., Kim, S., Rhie, J., Lee, S.-H., Kim, Y., & Kang, T.-S. (2018). Traveltimes data used in “Imaging of Lithospheric Structure Beneath Jeju Volcanic Island by Teleseismic Traveltimes Tomography”. Figshare. Fileset. <https://doi.org/10.6084/m9.figshare.6149858.v1>
- Takada, A. (1989). Magma transport and reservoir formation by a system of propagating cracks. *Bulletin of Volcanology*, 52(2), 118–126. <https://doi.org/10.1007/BF00301551>

- Tang, Y., Obayashi, M., Niu, F., Grand, S. P., Chen, Y. J., Kawakatsu, H., et al. (2014). Changbaishan volcanism in Northeast China linked to subduction-induced mantle upwelling. *Nature Geoscience*, 7(6), 470–475. <https://doi.org/10.1038/ngeo2166>
- Tatsumi, Y., Shukuno, H., Yoshikawa, M., Chang, Q., Sato, K., & Lee, M. W. (2005). The petrology and geochemistry of volcanic rocks on Jeju Island: Plume magmatism along the Asian continental margin. *Journal of Petrology*, 46(3), 523–553. <https://doi.org/10.1093/petrology/egh087>
- Thurber, C. H. (2003). Seismic tomography of the lithosphere with body waves. *Pure and Applied Geophysics*, 160(3), 717–737. <https://doi.org/10.1007/PL000012555>
- Thybo, H., & Artemieva, I. M. (2013). Moho and magmatic underplating in continental lithosphere. *Tectonophysics*, 609, 605–619. <https://doi.org/10.1016/j.tecto.2013.05.032>
- Valentine, G. A., & Perry, F. V. (2007). Tectonically controlled, time-predictable basaltic volcanism from a lithospheric mantle source (central basin and Range Province, USA). *Earth and Planetary Science Letters*, 261(1–2), 201–216. <https://doi.org/10.1016/j.epsl.2007.06.029>
- Van Wijk, J., Van Hunen, J., & Goes, S. (2008). Small-scale convection during continental rifting: Evidence from the Rio Grande rift. *Geology*, 36(7), 575–578. <https://doi.org/10.1130/G24691A.1>
- Van Wijk, J. W., Baldridge, W. S., Van Hunen, J., Goes, S., Aster, R., Coblenz, D. D., et al. (2010). Small-scale convection at the edge of the Colorado Plateau: Implications for topography, magmatism, and evolution of Proterozoic lithosphere. *Geology*, 38(7), 611–614. <https://doi.org/10.1130/G31031.1>
- Wang, X. C., Wilde, S. A., Li, Q. L., & Yang, Y. N. (2015). Continental flood basalts derived from the hydrous mantle transition zone. *Nature Communications*, 6(1), 7700. <https://doi.org/10.1038/ncomms8700>
- Wei, S. S., Wiens, D. A., Zha, Y., Plank, T., Webb, S. C., Blackman, D. K., et al. (2015). Seismic evidence of effects of water on melt transport in the Lau back-arc mantle. *Nature*, 518(7539), 395–398. <https://doi.org/10.1038/nature14113>
- Wei, W., Xu, J., Zhao, D., & Shi, Y. (2012). East Asia mantle tomography: New insight into plate subduction and intraplate volcanism. *Journal of Asian Earth Sciences*, 60, 88–103. <https://doi.org/10.1016/j.jseas.2012.08.001>
- Wei, W., Zhao, D., Xu, J., Zhou, B., & Shi, Y. (2016). Depth variations of *P* wave azimuthal anisotropy beneath Mainland China. *Scientific Reports*, 6(1), 29614. <https://doi.org/10.1038/srep29614>
- Wessel, P., Smith, W. H., Scharroo, R., Luis, J., & Wobbe, F. (2013). Generic Mapping Tools: Improved version released. *Eos*, 94(45), 409–410. <https://doi.org/10.1029/2013EO450001>
- West, J. D., Fouch, M. J., Roth, J. B., & Elkins-Tanton, L. T. (2009). Vertical mantle flow associated with a lithospheric drip beneath the Great Basin. *Nature Geoscience*, 2(6), 439–444. <https://doi.org/10.1038/ngeo526>
- Woo, Y., Yang, K., Kil, Y., Yun, S. H., & Arai, S. (2014). Silica- and LREE-enriched spinel peridotite xenoliths from the Quaternary intraplate alkali basalt, Jeju Island, South Korea: Old subarc fragments? *Lithos*, 208–209, 312–323. <https://doi.org/10.1016/j.lithos.2014.09.003>
- Yang, K., Hidas, K., Falus, G., Szabó, C., Nam, B., Kovács, I., & Hwang, B. (2010). Relation between mantle shear zone deformation and metasomatism in spinel peridotite xenoliths of Jeju Island (South Korea): Evidence from olivine CPO and trace elements. *Journal of Geodynamics*, 50(5), 424–440. <https://doi.org/10.1016/j.jog.2010.05.005>
- Yang, K., Szabó, C., Arai, S., Yu, J. E., & Jung, H. (2012). Silica enrichment of Group II xenoliths by evolved alkali basalt from Jeju Island, South Korea: Implication for modification of intraplate deep-seated rocks. *Mineralogy and Petrology*, 106(1–2), 107–130. <https://doi.org/10.1007/s00710-012-0222-x>
- Yoo, H. J., Herrmann, R. B., Cho, K. H., & Lee, K. (2007). Imaging the three-dimensional crust of the Korean Peninsula by joint inversion of surface-wave dispersion and teleseismic receiver functions. *Bulletin of the Seismological Society of America*, 97(3), 1002–1011. <https://doi.org/10.1785/0120060134>
- Zhang, M., Guo, Z., Cheng, Z., Zhang, L., & Liu, J. (2014). Late Cenozoic intraplate volcanism in Changbai volcanic field on the border of China and North Korea: Insights into deep subduction of the Pacific slab and intraplate volcanism. *Journal of the Geological Society*, 172(5), 648–663. <https://doi.org/10.1144/jgs2014-080>
- Zhao, D., Tian, Y., Lei, J., Liu, L., & Zheng, S. (2009). Seismic image and origin of the Changbai intraplate volcano in East Asia: Role of big mantle wedge above the stagnant Pacific slab. *Physics of the Earth and Planetary Interiors*, 173(3–4), 197–206. <https://doi.org/10.1016/j.pepi.2008.11.009>
- Zhao, D., Yamamoto, Y., & Yanada, T. (2013). Global mantle heterogeneity and its influence on teleseismic regional tomography. *Gondwana Research*, 23(2), 595–616. <https://doi.org/10.1016/j.gr.2012.08.004>
- Zheng, Y., Shen, W., Zhou, L., Yang, Y., Xie, Z., & Ritzwoller, M. H. (2011). Crust and uppermost mantle beneath the North China Craton, northeastern China, and the Sea of Japan from ambient noise tomography. *Journal of Geophysical Research*, 116, B12312. <https://doi.org/10.1029/2011JB008637>